

## On modeling turbulent exchange in buoyancy-driven fronts

Gustavo M. Marques\*, Tamay M. Özgökmen

RSMAS, University of Miami, Miami, FL, United States



### ARTICLE INFO

#### Article history:

Received 5 November 2013

Received in revised form 7 August 2014

Accepted 19 August 2014

Available online 6 September 2014

#### Keywords:

LES

OGCM

Mixing

Stirring

Submesoscale

### ABSTRACT

Our primary objective is to quantify the uncertainty in the solution space associated with mixing and stirring in ocean general circulation models (OGCMs) due to common modeling choices, namely the spatial resolution, tracer advection schemes, Reynolds number and turbulence closures. In many cases the assessment of errors is limited by the observational data set, therefore, large eddy simulations from a spectral element Boussinesq solver are taken as ground truth. First, the lock-exchange problem is used to quantify the temporal evolution of mixing from shear-driven stratified overturns. It is found that mixing in an OGCM is more sensitive to the choice of grid resolution than any other parameters tested here. The results do not monotonically converge towards the ground truth as the resolution is refined. Second, stirring of a passive tracer by submesoscale eddies generated by surface density fronts is considered. We find that using a second-order turbulence closure leads to an accurate representation of the restratification in the mixed layer.

© 2014 Elsevier Ltd. All rights reserved.

### 1. Introduction

Ocean general circulation models (OGCMs) are the primary tools for predicting ocean currents and changes in the ocean's stratification. Many OGCMs integrate the hydrostatic primitive equations (PE) set using a variety of horizontal and vertical coordinates, mixing parameterizations and advection schemes (e.g., Griffies et al., 2000, 2004). OGCMs have experienced significant development over the past two decades (Chassignet et al., 2006; Capet et al., 2008; Martin et al., 2009; Fox-Kemper and Menemenlis, 2008; Lemarié et al., 2012). These models can be configured at the global and regional scale, or can have a nested structure to represent multi-scale interactions (Debreu et al., 2012). Modern OGCMs contain realistic forcing, domain geometry, and assimilate ocean data available from a wide range of instruments, including (but not limited to) satellite altimeter, sea surface temperature, current meters, drifters and other *in situ* data for temperature and salinity.

The progress in OGCM development has been facilitated by the operational needs of the Navy as well as those of the basic research community (Shchepetkin and McWilliams, 1998; Hurlburt et al., 2009). Ocean observing and assimilation techniques have matured to a level where one can claim that the dynamics, phase and strength of the ocean's mesoscale features are adequately

represented in OGCMs. For instance, Thoppil et al. (2011) show that the energetics of the mesoscale field observed by drifters and satellite can be reproduced by both data-assimilative and non-assimilative models using a horizontal resolution of 1/12°–1/25°. Operational OGCMs can also exhibit a good predictive skill for the turn over time scales of mesoscale eddies (Hurlburt et al., 2008).

Nevertheless, OGCMs may encounter significant obstacles for reproducing accurate results for scales smaller and faster than the mesoscale (scales smaller than  $O(10)$  km and shorter than a few days) due primarily to three reasons. First, data at such scales may not be available from observing systems, or contain technical challenges within the context of present assimilation methods. For instance, sea-surface height data is usually converted to velocity under the assumption of geostrophy, while submesoscale flows are distinctly ageostrophic (Mahadevan and Tandon, 2006; Thomas et al., 2008).

Second, OGCMs may not resolve submesoscale features fully and must rely on subgrid-scale (SGS) parameterizations (Fox-Kemper et al., 2008; Fox-Kemper and Ferrari, 2008). Recent numerical studies showed that the SGS parameterization can have important consequences in the temporal and spatial evolution of submesoscale instabilities even when the grid spacing resolves the submesoscale (Ramachandran et al., 2013). OGCMs were originally designed to model large scales processes (i.e., on the order of the radius of deformation), where the flow is anisotropic with lateral processes being far more energetic than vertical processes. Therefore, these models sub-divide the SGS parameterizations for

\* Corresponding author.

E-mail addresses: [gmarques@rsmas.miami.edu](mailto:gmarques@rsmas.miami.edu) (G.M. Marques), [tozgokmen@rsmas.miami.edu](mailto:tozgokmen@rsmas.miami.edu) (T.M. Özgökmen).

the transport of momentum and tracers to whether they occur in the horizontal or vertical directions. In both cases, the unresolved processes are represented through an eddy viscosity or diffusivity. The vertical SGS models commonly used in OGCMs were originally designed for situations where turbulent processes are not even partially resolved and, therefore, the model resolution does not appear explicitly. These models fall into two basic categories: algebraic models, like KPP (K-Profile Parameterization, Large et al. (1994)) and second order turbulence closures (Large, 1998; Canuto et al., 2001). While there have been criticisms of KPP for needing tuning of dimensional parameters for different flows (Chang et al., 2005), the KPP algorithm has appeal not only because of its simplicity, but also because it has been shown to work reasonably well in challenging flows involving fully 3D stratified mixing affected by the details of bottom topography (Chang et al., 2008) within the limitations of the observational data sets. Second order turbulence closures have a long history of development (Mellor and Yamada, 1982; Kantha and Clayson, 1994; Burchard and Baumert, 1995; Burchard and Bolding, 2001; Canuto et al., 2001; Baumert and Peters, 2004; Baumert et al., 2005; Warner et al., 2005b; Umlauf and Burchard, 2005; Canuto et al., 2007), and they have also been shown to work reasonably well in complex problems involving shear-driven stratified mixing (e.g., the correct representation of mixing between overflows and ambient water masses; Ilcik et al., 2008). These models have a higher computational cost than algebraic models, since they require integration of two additional prognostic equations (typically turbulent kinetic energy and dissipation rate), as well as include significant assumptions on the form of these equations (Wilcox, 1998). Both classes of SGS models are aimed to estimate a diffusivity coefficient, parameterizing only the downward energy cascade processes. Parameterizations that potentially address upward energy cascade, or dispersion (as opposed to dissipation) potentially exist (San et al., 2011; Berselli et al., 2011), but have not been extensively investigated yet.

Third, even if the OGCMs contain the spatial resolution to extend into the submesoscales and below, the PE start losing validity, being subject to the hydrostatic approximation (Kantha and Clayson, 2000). The hydrostatic approximation affects both dissipative and dispersive properties of fluid motion. Neither the overturning of density surfaces by Kelvin–Helmholtz (KH) instability, which is one of the primary mechanisms responsible for mixing in the ocean (McWilliams, 2008; Taylor and Ferrari, 2009), nor the correct dispersion relation for non-linear internal waves can be explicitly captured with hydrostatic models. Since the inclusion of a non-hydrostatic pressure solver in OGCMs requires a substantial change in these codes, recent efforts have focussed on the development of suitable solvers (Scotti and Mitran, 2008) and hybrid hydrostatic and non-hydrostatic models (Botelho et al., 2009; Duan et al., 2010; Campin et al., 2010). As both of these avenues will not only require significant code development, but also will generate substantially larger model output for post-analysis, there is still need for further investigations within the formalism of the existing OGCMs.

To conclude, there is a need for carefully evaluating the accuracy of the OGCMs (and their SGS models) below the mesoscale regime. The scales of interest include submesoscales, as well as fully 3D stratified mixing.

The submesoscale phenomena were first recognized by McWilliams (1985) and received considerable attention in recent years, with the identification of mixed-layer instability (Boccaletti et al., 2007; Fox-Kemper et al., 2008) and the importance of submesoscale motions in biogeochemical transport in the ocean (Lévy et al., 2001; Klein and Lapeyre, 2009; Calil and Richards, 2010). In addition, submesoscale motions are thought to form the bridge between long-lived quasi-geostrophic motions

and rapidly-dissipating small scale turbulence (Müller et al., 2005; McWilliams, 2008; Capet et al., 2008). Stratified mixing is of interest in coastal phenomena (Warner et al., 2005a; MacCready et al., 2009), as well as during deep water formation (Legg et al., 2009). Therefore, it is critical that OGCMs represent stratified mixing accurately, or alternatively, the errors associated with their parametric representation are quantified.

Here, we present a direct comparison of results from two types of problems that are challenging for OGCMs:

- (1) So-called lock-exchange (LE) problem, which is a simple computational setting to quantify the temporal evolution of mixing in a stratified fluid. This problem is discussed in some detail by Özgökmen et al. (2009a,b).
- (2) Mixed-layer instability (MLI) for submesoscale motions. MLI is very similar to the LE problem in terms of the computational setting, but differs dynamically due to the presence of ambient rotation and a high-aspect domain ratio. MLI was studied using LES by Özgökmen et al. (2011, 2012) and Özgökmen and Fischer (2012). The metric of interest here is the lateral stirring carried out by the submesoscale MLI eddies. This is of relevance to the lateral dispersion of pollutants and biogeochemical tracers in the ocean.

While computations for both problems are carried out in idealized settings, they have the advantage that LES (large eddy simulation, Sagaut (2006)) solutions are feasible and serve as ground truth. LES refers to numerical solutions of the non-hydrostatic equations in which the large eddies, carrying most of the Reynolds stresses, are resolved through computation, while the effect of the smaller eddies on the flow is represented by SGS models that depend explicitly on the resolution of the model. The goal of these SGS models is to anticipate higher resolution results at any given resolution (hence simulations performed using LES will converge as resolution is increased). The LES approach lies in between the extremes of direct numerical simulation (DNS), where all turbulence is resolved, and Reynolds-averaged Navier–Stokes (RANS), in which only the mean flow is computed while the entire effect of turbulence is represented by SGS models (such as the second order turbulence closures). Since LES greatly reduces the SGS parameterization problem, many studies on ocean turbulence have relied on this approach to establish a ground truth for particular problems (Wang et al., 1998; Large, 1998; Chang et al., 2005; Xu et al., 2006). In addition, recent studies (Fox-Kemper and Menemenlis, 2008; Ramachandran et al., 2013) have shown that LES techniques can replace the traditional RANS methods and are a promising avenue for SGS parameterizations in high-resolution ocean models.

The paper is organized as follows. Section 2 gives a brief introduction on the numerical models used in this study. In Sections 3 and 4, models configuration, experimental description, metrics employed and results are presented for the LE and the MLI problems, respectively. The principal findings are summarized in Section 5.

## 2. The numerical models

### 2.1. LES model – Nek5000

Our reference model is Nek5000, which integrates the Boussinesq equations (BE) based on the spectral element method, a high order finite element method for partial differential equations (Patera, 1984; Fischer, 1997). Nek5000 has been previously used for oceanic applications relevant to mixing and stirring, such as LES of LE problem (Özgökmen et al., 2007, 2009a,b) as well as

LES of MLI (Özgökmen et al., 2011, 2012; Özgökmen and Fischer, 2012). High-order spectral element methods have significantly better convergence characteristics than finite difference methods, leading to negligible numerical dissipation and errors (Patera, 1984; Fischer et al., 1988; Boyd, 2001).

Nek5000 is configured to integrate the non-dimensionalized Boussinesq equations:

$$\begin{cases} \frac{D\bar{\mathbf{u}}}{Dt} = Ro_H^{-1} \hat{\mathbf{z}} \times \bar{\mathbf{u}} - \nabla \bar{p} - Fr^{-2} \bar{\rho}' \hat{\mathbf{z}} + Re^{-1} \nabla^2 \bar{\mathbf{u}} - \nabla \cdot \boldsymbol{\tau}, \\ \nabla \cdot \bar{\mathbf{u}} = 0, \\ \frac{D\bar{\rho}'}{Dt} = Pe^{-1} \nabla^2 \bar{\rho}', \\ \frac{D\bar{C}}{Dt} = Pe^{-1} \nabla^2 \bar{C}, \end{cases} \quad (1)$$

where the flow variables are the velocity vector  $\mathbf{u}$ , pressure  $p$ , density perturbation  $\rho'$  and passive tracer concentration  $C$ . The non-dimensional parameters are the Reynolds number  $Re = U_0 H_0 / v$ , the Froude number  $Fr = U_0 / (NH_0)$ , the vertical Rossby number  $Ro_H = U_0 / (fH_0) = aRo$ , where  $Ro = U_0 / (fL)$  is the Rossby number,  $a = L/H_0$  is the ratio of horizontal and vertical domain sizes and the Peclet number  $Pe = U_0 H_0 / \kappa$ . The latter can also be written as  $Pe = RePr$ , where  $Pr = v/\kappa$  is the Prandtl number.  $U_0$  is the flow speed scale,  $H_0$  the total fluid depth,  $v$  is the kinematic viscosity,  $\kappa$  is the molecular diffusivity,  $g$  is the gravitational acceleration,  $\rho_0$  is the fluid density,  $N$  is the buoyancy frequency,  $f$  is the Coriolis frequency and  $\hat{\mathbf{z}}$  is the unit vector in the vertical direction.

In (1),  $\frac{D}{Dt} := \frac{\partial}{\partial t} + \bar{\mathbf{u}} \cdot \nabla$  is the material derivative and overbars indicate resolved fields by constraining the spatial filtering to the computational mesh. In all Nek5000 simulations presented here, the subgrid scale tensor  $\boldsymbol{\tau} = \bar{\mathbf{u}}\bar{\mathbf{u}} - \bar{\mathbf{u}}\bar{\mathbf{u}}$  is computed using a dynamic Smagorinsky model. No explicit subgrid models are used for the density perturbation and tracer concentration fields, relying instead on de-aliasing and high-order filtering operations. For brevity here, the reader is referred to Özgökmen et al. (2009a,b) for further details on the dynamic Smagorinsky model.

## 2.2. OGCM – ROMS

The Regional Ocean Modeling System (ROMS<sup>1</sup>) is a three-dimensional, free-surface, hydrostatic, primitive equation ocean model formulated in a terrain-following vertical coordinate (Song and Haidvogel, 1994; Shchepetkin and McWilliams, 2005; Haidvogel et al., 2008). We emphasize that this is a widely used community model and, therefore, a fair choice to represent commonly used OGCMs. The horizontal discretization is by an orthogonal curvilinear Arakawa-C grid. In Cartesian coordinates, the horizontal momentum equations solved by ROMS in this particular study are:

$$\begin{aligned} \frac{\partial u}{\partial t} + \mathbf{u} \cdot \nabla u - fv &= -\frac{1}{\rho_0} \frac{\partial \phi}{\partial x} + F_u + K_{MH} \nabla^2 u \\ &\quad + \frac{\partial}{\partial z} \left( K_{MV} \frac{\partial u}{\partial z} + v \frac{\partial u}{\partial z} \right), \end{aligned} \quad (2)$$

and

$$\begin{aligned} \frac{\partial v}{\partial t} + \mathbf{u} \cdot \nabla v + fu &= -\frac{1}{\rho_0} \frac{\partial \phi}{\partial y} + F_v + K_{MH} \nabla^2 v \\ &\quad + \frac{\partial}{\partial z} \left( K_{MV} \frac{\partial v}{\partial z} + v \frac{\partial v}{\partial z} \right), \end{aligned} \quad (3)$$

while the vertical momentum equation is replaced by the hydrostatic approximation:

$$\frac{\partial \phi}{\partial z} = -\frac{\rho' g}{\rho_0}. \quad (4)$$

The continuity and scalar transport equations follow

$$\frac{\partial u}{\partial x} + \frac{\partial v}{\partial y} + \frac{\partial w}{\partial z} = 0, \quad (5)$$

and

$$\frac{\partial T}{\partial t} + \mathbf{u} \cdot \nabla T = F_T + K_{CH} \nabla^2 T + \frac{\partial}{\partial z} \left( K_{CV} \frac{\partial T}{\partial z} + v_0 \frac{\partial T}{\partial z} \right). \quad (6)$$

A linear equation of state is used to be consistent with (1)

$$\rho = \rho_0 (1 - T_{coef}(T - T_0)). \quad (7)$$

In (2)–(7)  $F_u, F_v, F_C$  represent the forcing terms,  $\phi$  is the dynamic pressure,  $v$  and  $v_0$  are the background molecular viscosity and diffusivity, respectively,  $\rho_0 = 1025 \text{ kg m}^{-3}$  is the background density,  $T_{coef} = 2.06 \times 10^{-4} \text{ }^{\circ}\text{C}$  is the thermal expansion coefficient,  $T_0 = 5 \text{ }^{\circ}\text{C}$  is the background potential temperature,  $K_{MV}$  and  $K_{CV}$  are vertical eddy viscosity and diffusivity, while  $K_{MH}, K_{CH}$  are horizontal eddy viscosity and diffusivity, respectively.

For both idealized cases studied here, the horizontal momentum is discretized with a third-order, upstream-biased advection scheme with velocity dependent hyper-viscosity (Shchepetkin and McWilliams, 1998). This scheme allows the generation of steep gradients in the solution, enhancing the effective resolution of the solution for a given grid size when the explicit viscosity is small. The implicit numerical diffusion, which acts as implicit viscosity, is such that the effective horizontal Reynolds number at that grid resolution takes the largest value possible while still ensuring adequate dissipation for stability. The latter is particularly useful in reducing spurious mixing (Ilicak et al., 2012). For the vertical momentum, a fourth-order centered differences scheme is used. Horizontal mixing of momentum and tracers is computed using a Laplacian formulation. Further details on the model configuration for each idealized application are described next.

## 3. Lock exchange problem for stratified mixing

### 3.1. Model configurations and parameters

For this problem we ignore the rotational terms in Eqs. (1)–(3). Since both models integrate a different set of equations of motion, it is not a trivial matter to set them up in an identical fashion. We focus on some of the issues that require care in setting up these models. While Nek5000 configuration is based on the non-dimensional numbers  $a, Fr, Pr$  and  $Re$  (defined in Section 2.1), ROMS is configured in terms of dimensional variables. Another important difference between these models within the context of the present set of comparisons is that ROMS splits viscosity/diffusion in horizontal and vertical, and these coefficients parameterize most of the mixing, while in the LES model Nek5000 mixing is mostly represented by resolved turbulence and subgrid-scale parameterizations are of marginal influence.

For the LE, Nek5000 is configured exactly as described in Özgökmen et al. (2009b), but here the model is run approximately four times longer to include later stages when the collapse of turbulence to internal waves become important. Although the mixing rate is significantly reduced after this transition, turbulence is not totally shut off and small amounts of mixing taking place over a long period can also be important. We summarize the selection of the non-dimensional parameters in (1) as:  $a = L/H_0 = 2, W/H_0 = 1$  (where  $W$  is the horizontal width in the domain),  $Fr = 2^{-\frac{1}{2}}$  and  $Pr = 7$ . The only remaining physical parameter of the problem is  $Re$  and we conduct LES simulations at two Reynolds numbers, namely  $Re = 10^3$  and  $Re = 10^4$ . These LES simulations are used as our ground truth. The reader is referred to experiments low-res2 ( $Re = 10^3$ ) and high-res2 ( $Re = 10^4$ )

<sup>1</sup> <http://www.myroms.org/>.

described in Özgökmen et al., 2009b for additional details on these simulations.

In ROMS, the horizontal and vertical length scales are set to  $L = 200$  and  $H = 100$  m, respectively, given an aspect ratio of  $a = 2$ . The width of the domain is set to  $W = 100$  m. The Froude number  $Fr$  is the ratio between the characteristic advection speed, defined as  $U_0 = \frac{1}{2} \sqrt{g\Delta\rho H/\rho_0}$  (Özgökmen et al., 2009b), and the internal wave speed, defined as  $\sqrt{g\Delta\rho l/\rho_0}$ , where  $l = H/2 = 50$  m. Thus, for this configuration  $Fr = 2^{-\frac{1}{2}}$  regardless of the choice for the density perturbation ( $\rho'$ ). As shown in Section 2.2, ROMS separates viscosity/diffusivity in vertical and horizontal. Therefore, we introduce  $Pr_V$  ( $Re_V$ ) and  $Pr_H$  ( $Re_H$ ) as the vertical and horizontal Prandtl (Reynolds) numbers, respectively. The values of the explicit  $Re_H$  used in this study are listed in Table 1. Although we set  $Pr_H = 7$  (i.e., momentum diffuses seven times faster than heat in the horizontal), we cannot guarantee that  $K_{CH}$  is always larger than the numerical diffusion from the tracer advection scheme (hence, it is more appropriate to say that  $Pr_H \leq 7$ ). Additional inconsistency between Nek5000 and ROMS is the fact that both  $Pr_V$  and  $Re_V$  are controlled by the turbulent closure. The reason is that  $K_{MV}$  and  $K_{CV}$  are set according to the schemes of each closure. Nevertheless, we conduct three control experiments where  $K_{MV}$  and  $K_{CV}$  are set analytically to constant values (more details in Section 3.2).

At the northern and southern sides, periodic boundary conditions are applied, while at the eastern and western walls no-flow and free-slip boundary conditions are used. The effects of bottom friction are ignored (i.e.,  $C_D = 0$ ).

The LE problem is initialized with dense fluid on the left separated from light fluid on the right:

$$\frac{\rho'(x,y,z,0)}{\Delta\rho'} = \begin{cases} 1 & \text{for } 0 \leq x < (L/2 + \eta), \\ 0 & \text{for } (L/2 + \eta) \leq x \leq L, \end{cases} \quad (8)$$

where  $\eta$  is a function that defines the perturbation to be superimposed on the density interface to generate 3D flows. For the LE experiments presented in the following section a perturbation of the form  $\eta = 10 \times \sin(\pi y/W)$  is used. A similar perturbation is employed in Özgökmen et al. (2009b). The system starts from a state of rest,  $\mathbf{u} = 0$ , and it is integrated until the rate of stratified mixing becomes negligible with respect to the initial vigorous activity. One important time scale for the system is the time it takes for the internal gravity currents to cross the domain  $T_p = L/U_0$ . The total integration period ( $T$ ) needs to be much larger than  $T_p$  for

the effects of stratification to fully develop. Both ROMS and Nek5000 simulations are integrated until non-dimensional time of  $t^* = 4 \times T/T_p \approx 60$ .

### 3.2. List of experiments and quantification of mixing

**Table 1** presents the set of sixteen LE experiments conducted with different configurations in terms of: (i) grid resolution, (ii) choice of turbulence closures (with the values of vertical background viscosity  $K_{MV}^0$  and diffusivity  $K_{CV}^0$  used when using KPP-Ri, see more details below), (iii) tracer advection scheme and (iv) explicit horizontal Reynolds number ( $Re_H$ ). The following rationale is used when specifying the simulation names (e.g., le-10-ke-10<sup>3</sup>): type of problem – grid resolution ( $\Delta x = \Delta y = \Delta z$ ) – turbulence closure, or tracer advection scheme, or absence of vertical mixing (novmix), or fixed  $K_{MV}$  and  $K_{CV}$  values (ctrl) –  $Re_H$  value.

The main purpose of changing spatial resolution is to examine the sensitivity of the results on grid resolution. Ideally, resolution-independent results would be desirable. Four values are tested here: 10, 5, 2.5 and 1.25 m. We assure that in all experiments run at  $Re_H = 10^3$  the implicit numerical diffusion (which acts as implicit viscosity), in the advection operator, is smaller than the explicit horizontal eddy viscosity ( $K_{MH}$ ). Appendix A provides further details on how the latter is verified, using simulations with 10 m resolution as example and based on an asymptotic analysis similarly to that employed in Dong et al. (2007). We should point out that in the experiments run at  $Re_H = 10^4$  the implicit horizontal numerical diffusion approaches the explicit  $K_{MH}$  and, therefore, we have no control over  $Re_H$  (even though we state that  $Re_H = 10^4$  in those experiments). Nevertheless, we use these simulations to show that the results become completely independent to the choice of turbulence closure when the effective  $Re_H$  is large and entirely controlled by numerical diffusion.

To investigate the effects of tracer advection schemes on mixing, we run experiment le-2.5-u3h-10<sup>3</sup>, where a combination of third-order upstream-biased horizontal scheme (U3H) and fourth-order centered vertical scheme (C4V) is used. All the other experiments are carried out using the multidimensional positive definite advection transport algorithm (MPDATA). The MPDATA algorithm conserves mass and it preserves the positive-definite characteristics of the tracers, which avoids under- and overshooting of the initial tracer values. The sensitivity of mixing on the explicit horizontal Reynolds number ( $Re_H$ ) is assessed by running

**Table 1**

List of LE experiments conducted with ROMS. The number of grid points in the  $x$ ,  $y$  and  $z$  directions are:  $20 \times 10 \times 10 = 2000$  for  $\Delta x = \Delta y = \Delta z = 10$  m,  $40 \times 20 \times 20 = 16,000$  for  $\Delta x = \Delta y = \Delta z = 5$  m,  $80 \times 40 \times 40 = 128,000$  for  $\Delta x = \Delta y = \Delta z = 2.5$  m, and  $160 \times 80 \times 80 = 1,024,000$  for  $\Delta x = \Delta y = \Delta z = 1.25$  m. CA = Canuto-A stability function, and  $K_{MV}$  ( $K_{MV}^0$ ) and  $K_{CV}$  ( $K_{CV}^0$ ) are the vertical (background) viscosity and diffusivity, respectively. The symbol \* indicates that a combination of third-order upstream-biased horizontal scheme and fourth-order centered vertical scheme has been used.

| Experiment                     | $\Delta x$ (m) | $Re_H$          | Turb. closure | $K_{CV}^0$ ( $m^2 s^{-1}$ ) | $K_{MV}^0$ ( $m^2 s^{-1}$ ) |
|--------------------------------|----------------|-----------------|---------------|-----------------------------|-----------------------------|
| le-10-ke-10 <sup>3</sup>       | 10             | 10 <sup>3</sup> | k-ε/CA        |                             |                             |
| le-10-kpp-10 <sup>3</sup>      | 10             | 10 <sup>3</sup> | KPP-Ri        | $1.60 \times 10^{-3}$       | $1.12 \times 10^{-2}$       |
| le-5-ke-10 <sup>3</sup>        | 5              | 10 <sup>3</sup> | k-ε/CA        |                             |                             |
| le-5-kpp-10 <sup>3</sup>       | 5              | 10 <sup>3</sup> | KPP-Ri        | $1.60 \times 10^{-3}$       | $1.12 \times 10^{-2}$       |
| le-2.5-ke-10 <sup>3</sup>      | 2.5            | 10 <sup>3</sup> | k-ε/CA        |                             |                             |
| le-2.5-kpp-10 <sup>3</sup>     | 2.5            | 10 <sup>3</sup> | KPP-Ri        | $1.60 \times 10^{-3}$       | $1.12 \times 10^{-2}$       |
| le-2.5-u3h-10                  | 2.5            | 10 <sup>3</sup> | k-ε/CA        |                             |                             |
| le-1.25-ke-10 <sup>3</sup>     | 1.25           | 10 <sup>3</sup> | k-ε/CA        |                             |                             |
| le-1.25-kpp-10 <sup>3</sup>    | 1.25           | 10 <sup>3</sup> | KPP-Ri        | $1.60 \times 10^{-3}$       | $1.12 \times 10^{-2}$       |
| le-1.25-ke-10 <sup>4</sup>     | 1.25           | 10 <sup>4</sup> | k-ε/CA        |                             |                             |
| le-1.25-kpp-10 <sup>4</sup>    | 1.25           | 10 <sup>4</sup> | KPP-Ri        | $1.60 \times 10^{-4}$       | $1.12 \times 10^{-3}$       |
|                                |                |                 |               | $K_{CV}$ ( $m^2 s^{-1}$ )   | $K_{MV}$ ( $m^2 s^{-1}$ )   |
| le-1.25-ctrl-10 <sup>3</sup>   | 1.25           | 10 <sup>3</sup> | none          | $1.60 \times 10^{-3}$       | $1.12 \times 10^{-2}$       |
| le-1.25-ctrl-10 <sup>4</sup>   | 1.25           | 10 <sup>4</sup> | none          | $1.60 \times 10^{-4}$       | $1.12 \times 10^{-3}$       |
| le-1.25-novmix-10 <sup>3</sup> | 1.25           | 10 <sup>3</sup> | none          | 0                           | 0                           |

experiments at two  $Re_H$  values ( $10^3$  and  $10^4$ ). Finally, the effects of turbulence closures on mixing are investigated by selecting two popular models:

1. The algebraic K-Profile Parameterization model (KPP) (Large et al., 1994). Here, only the component due to resolved vertical shear is considered. Shear-driven mixing is expressed in terms of the local gradient Richardson number,

$$Ri_g = N^2 \left[ \left( \frac{\partial u}{\partial z} \right)^2 + \left( \frac{\partial v}{\partial z} \right)^2 \right]^{-1}, \quad (9)$$

which is the ratio between the buoyancy frequency and the vertical shear. Vertical eddy viscosity is then estimated as:

$$K_{MV} = \begin{cases} K_{MV}^0 & \text{for } Ri_g < 0, \\ K_{MV}^0 [1 - (Ri_g/Ri_0)^2]^3 & \text{for } 0 < Ri_g < Ri_0, \\ 0 & \text{for } Ri_g > Ri_0, \end{cases} \quad (10)$$

where  $Ri_0 = 0.7$ . Eq. (10) is also used to compute  $K_{CV}$ , but a background diffusivity coefficient ( $K_{CV}^0$ ) is used instead of that for viscosity ( $K_{MV}^0$ ). These coefficients are prescribed by the user and the values used in our LE runs are listed in Table 1.

2. The two-equation standard k- $\varepsilon$  closure (Burchard and Baumert, 1995) for stratified flow with Canuto-A stability function (Canuto et al., 2001). We choose k- $\varepsilon$ /CA based on a recent evaluation of turbulence closures in three-dimensional simulations of the Red Sea overflow (Ilicak et al., 2008). The k- $\varepsilon$  model uses transport equations for turbulent kinetic energy (TKE) and the dissipation rate  $\varepsilon$  of the TKE, while the Canuto-A stability function includes the effects of shear and stratification. Unlike the shear-driven mixing in KPP, the user does not need to prescribe the value of any coefficient in this closure. The reader is referred to Warner et al. (2005b) (and references therein) for a complete description of k- $\varepsilon$ /CA and their implementation in ROMS.

Additionally, three control experiments where both  $K_{MV}$  and  $K_{CV}$  are set to fixed values (no turbulence closure is used) are conducted. In experiment le-1.25-ctrl- $10^3$  we set  $K_{MV} = 1.12 \times 10^{-2} \text{ m}^2 \text{ s}^{-1}$  and  $K_{CV} = 1.60 \times 10^{-3} \text{ m}^2 \text{ s}^{-1}$ , while in experiment le-1.25-ctrl- $10^4$  these parameters are set to  $1.12 \times 10^{-3} \text{ m}^2 \text{ s}^{-1}$  and  $1.60 \times 10^{-4} \text{ m}^2 \text{ s}^{-1}$ , respectively (see Table 1). Experiment le-1.25-novmix- $10^3$  is intended to explore the absence of vertical mixing ( $K_{MV} = K_{CV} = 0$ ) on the system while keeping  $Re_H = 10^3$ .

In ROMS, the baroclinic time step is set to  $\Delta x/500$  s and the number of barotropic time steps between each baroclinic time step is set to 20. This yields a maximum lateral CFL number of  $8.8 \times 10^{-2}$  for all simulations. ROMS experiments are conducted on University of Miami's Linux cluster (IBM iDataPlex dx360M4) based on 16 Intel Sandy Bridge 2.6 GHz cores, 32 GB of RAM and infiniBand clustering network, while Nek5000 experiments have been carried out on a Cray XE6m machine at the City University of New York High-Performance Computer Center.<sup>2</sup> ROMS and Nek5000 scale at approximately  $1.5 \times 10^4$  and  $5.10 \times 10^3$  grid points per node, respectively. The number of nodes for each experiment as well as the wall clock time for an integration  $t^* \approx 60$  are listed in Table 2.

For this application, the metric used is the background (or reference) potential energy (BPE), which quantifies mixing in a enclosed system (Winters et al., 1995), such as the lock-exchange domain employed here. BPE is defined as the minimum potential energy that can be obtained through an adiabatic redistribution of the water masses. Mixing increases the BPE, since it provides a direct measure of the potential energy changes due to irreversible

**Table 2**

Wall clock time and the number of nodes used in the LE and MLI experiments.

| Experiment                       | # of nodes | Wall clock time (hours) |
|----------------------------------|------------|-------------------------|
| le-10-k $\varepsilon$ - $10^3$   | 1          | 0.1                     |
| le-10-kpp- $10^3$                | 1          | 0.1                     |
| le-5-k $\varepsilon$ - $10^3$    | 1          | 0.9                     |
| le-5-kpp- $10^3$                 | 1          | 0.7                     |
| le-2.5-k $\varepsilon$ - $10^3$  | 8          | 2.2                     |
| le-2.5-kpp- $10^3$               | 8          | 1.5                     |
| le-2.5-u3h- $10^3$               | 8          | 1.2                     |
| le-1.25-k $\varepsilon$ - $10^3$ | 32         | 16.5                    |
| le-1.25-kpp- $10^3$              | 32         | 10.4                    |
| le-1.25-k $\varepsilon$ - $10^4$ | 32         | 20.2                    |
| le-1.25-kpp- $10^4$              | 32         | 14.1                    |
| le-1.25-ctrl- $10^3$             | 32         | 13.1                    |
| le-1.25-ctrl- $10^4$             | 32         | 13.2                    |
| le-1.25-novmix- $10^3$           | 32         | 13.2                    |
| le-LES ( $10^3$ )                | 16         | 308                     |
| le-LES ( $10^4$ )                | 384        | 48,000                  |
| mli-100-32-k $\varepsilon$       | 16         | 2.3                     |
| mli-200-32-k $\varepsilon$       | 4          | 0.7                     |
| mli-50-32-k $\varepsilon$        | 64         | 4.7                     |
| mli-100-16-k $\varepsilon$       | 4          | 2.9                     |
| mli-100-64-k $\varepsilon$       | 36         | 2.0                     |
| mli-100-32-kpp                   | 16         | 1.5                     |
| mli-100-32-novmix                | 16         | 1.4                     |
| mli-LES                          | 256        | 192                     |

diapycnal mixing. This metric has been widely used to compute mixing in numerical simulations of turbulent flows (Winters et al., 1995; Tseng and Ferziger, 2001; Özgökmen et al., 2007, 2009a,b; Ilicak et al., 2009, 2012) and the reader is referred to Özgökmen et al. (2007, Fig. 5 and associated text) for a detailed discussion on how changes in BPE relate to diapycnal mixing in the LE problem.

We follow the technique introduced by Tseng and Ferziger (2001) to compute BPE using the probability density function. In our analysis the density perturbation is split into 51 bins at each time step, and integrated:

$$BPE = gLW \int_0^H \rho'(z_r) z_r dz_r, \quad (11)$$

where  $z_r(\rho')$  is the height of fluid of density  $\rho'$  in the minimum potential energy state. The  $\rho'$  bins are fixed in time and vary between the minimum and maximum values at  $t^* = 0$  (0 and  $1 \text{ kg m}^{-3}$ , respectively). Therefore, the under- and over-shootings discussed in Section 3.4 are not included in the calculation of BPE. We present the results in terms of the non-dimensional background potential energy, defined as:

$$BPE^* = \frac{BPE(t^*) - BPE(t^* = 0)}{BPE(t^* = 0)}. \quad (12)$$

It is convenient to use Eq. (12) to visualize the relative increase of the BPE with respect to the initial state by mixing. We highlight that  $BPE^* \geq 0$  and it increases monotonically for physically realistic solutions.

### 3.3. Description of the flow

Since active tracer fields are a convenient way of visualizing stratified turbulent flows, we use the normalized density perturbation field ( $\rho'/\Delta\rho'$ ) to describe the evolution of the LE problem. We choose the results from experiments le-1.25-k $\varepsilon$ - $10^4$  (see Table 1) and the LES ( $Re = 10^4$ ) simulation to described the time evolution of  $\rho'/\Delta\rho'$ . At  $t^* = 4.1$  (Fig. 1(a) and (b)), mixing is enhanced when the two gravity currents, traveling in opposite directions, collide on the center of the domain. The three-dimen-

<sup>2</sup> <http://www.csi.cuny.edu/cunyhpc/>.

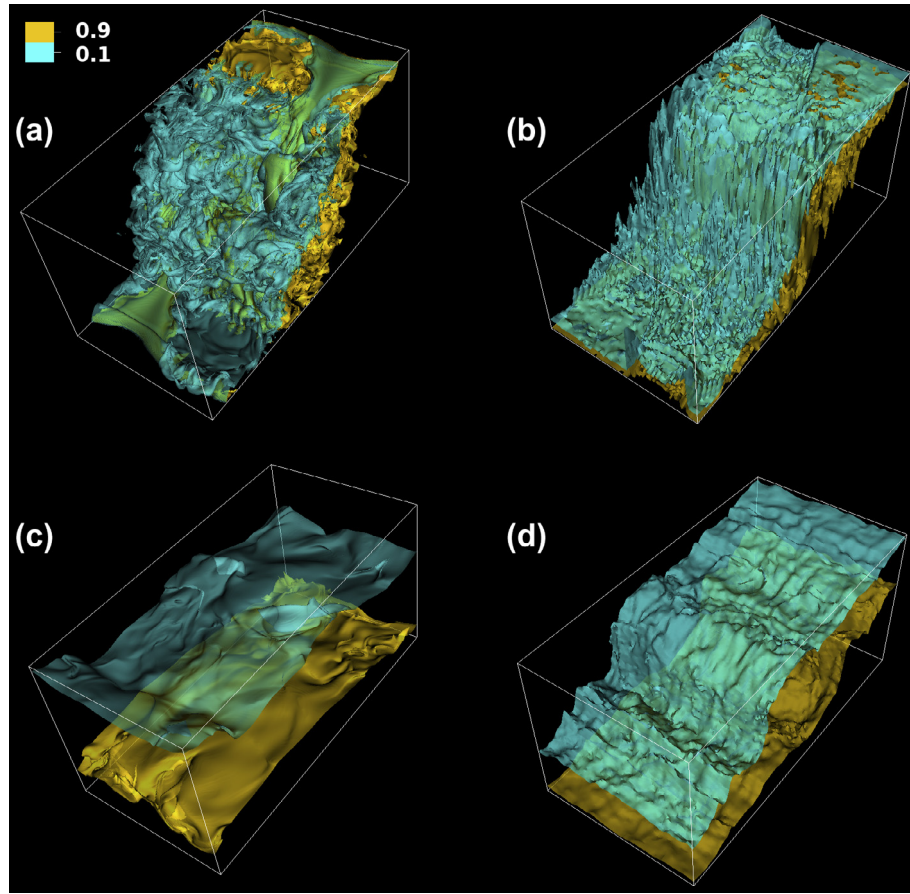


**Fig. 1.** Contours of the normalized density perturbation  $\rho'/\Delta\rho'$  values for the (left panels) Nek5000 simulation LES ( $Re = 10^4$ ) and (right panels) ROMS experiment le-1.25-ke- $10^4$  (see Table 1) during two non-dimensional times  $t^* = 4.1$  (a and b) and  $t^* = 47.6$  (c and d). The contours values are 0.1 (blue) and 0.9 (yellow). Animations of both the LES simulation (dbpri153.mov) and the ROMS simulation (le-1.25-ke-10000.mov) are available in the Auxiliary Materials. (For interpretation of the references to colour in this figure legend, the reader is referred to the web version of this article.)

sionality of the flow, resulting from the initial sinusoidal perturbation, is evident at this stage in both ROMS and LES simulations. The solution in the ROMS simulation is much less smooth than in the LES. As pointed out by Ilicak et al. (2012), the lock-exchange problem is characterized by noise divergencies in the horizontal velocities near the head of the counter-propagating gravity currents, which are related to large energy in the velocity at or near the horizontal grid scale. Although the momentum advection scheme used in ROMS has viscous dissipation built into it to ensure that the flow field is smooth at the grid scale (Shchepetkin and McWilliams, 1998), our results show that the effectiveness of this mitigation is reduced at small  $\Delta x$  and high  $Re_H$  (see following section for further discussion). Towards the end of the simulation (Fig. 1(c) and (d)) the density perturbation becomes smoother as shear decreases, while the density interface becomes thicker as a result of mixing. Due to the difference in the internal wave speed (dispersion) between the hydrostatic (ROMS) and the non-hydrostatic (LES) simulations, the flows no longer exhibit similar behavior (e.g., the position of gravity current fronts) as  $t^*$  increases (Fig. 1(c) and (d)). Although not explored in the present study, it is known that hydrostatic models cannot produce the correct dispersion for non-linear internal waves (Scotti and Mitrani, 2008). In addition, the choice of numerical schemes may also play an important role on the speed of internal waves (Hodges et al., 2006) and further studies should be done to address these issues. In the following sections we focus in quantifying mixing during the time evolution of the LE problem.

### 3.4. Comparison of mixing from LES and ROMS

In this section, the sensitivity of mixing to the modeling choices presented in Section 3.2 are explored.

Figs. 2 and 3 show the time evolution of the non-dimensional background potential energy  $BPE^*$  for all experiments listed in Table 1. Until  $t^* \approx 2$ , when the two counter-propagating gravity currents collide on the wall, the  $BPE^*$  curves in the different ROMS simulations are very similar and display larger mixing (and mixing rate) than the LES simulations. However, shortly after, the ROMS simulations display different patterns among themselves and, overall, there is a small decrease in the  $BPE^*$  slope. On the other hand, the mixing rate in the LES experiments is enhanced after the two gravity currents collide on the center of the domain ( $t^* \approx 4.1$ ).

Overall, the flow in both ROMS and LES follows two stages during the evolution of the LE problem. First, shear-driven mixing dominates and the mixing increases rapidly. Second (after  $t^* \approx 15$ ), a fairly abrupt change in the regime occurs when the collapse of turbulence to internal waves takes place. In all runs this occurs approximately right after the two gravity currents, traveling at opposite direction, collide on the center of the domain for the third time. The initial (shear-driven) mixing rate is reduced in simulations with  $\Delta x = 1.25$  m and, therefore, this collapse becomes less pronounced in these runs. Shear-driven mixing is now sparse (as shown by the smoother contours in Fig. 1(c) and (d), and corresponding animations) and the mixing rate decreases significantly during this last stage (Figs. 2 and 3).

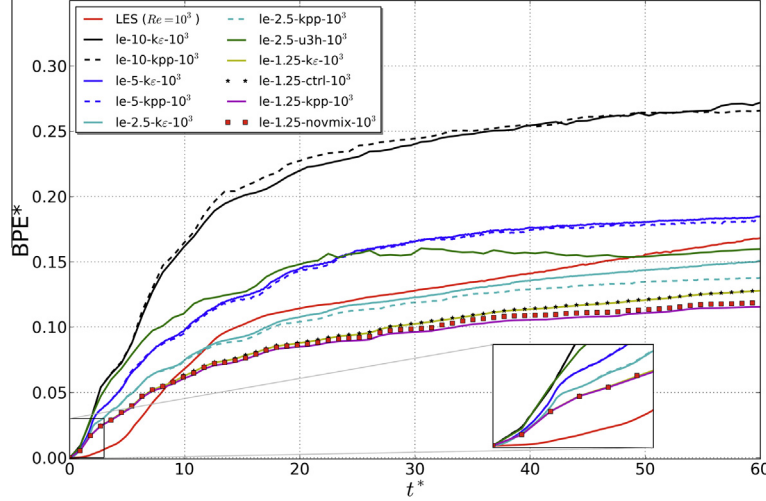


**Fig. 2.** Time evolutions of the normalized background potential energy  $BPE^*$  from experiments with  $\Delta x = 10, 5, 2.5$  and  $1.25$  m and  $Re_H = 10^3$ . The curve from the reference LES ( $Re = 10^3$ ) experiment is also shown for comparison. Note the overlap between curves from experiments  $le-1.25-ke-10^3$  and  $le-1.25-ctrl-10^3$ ; and  $le-1.25-kpp-10^3$  and  $le-1.25-novmix-10^3$ . The lower panel on the right shows an expanded plot of the initial evolution of  $BPE^*$ .

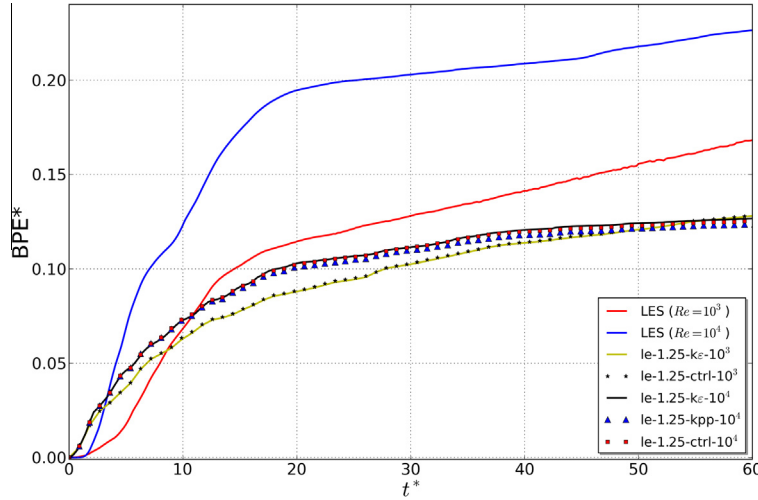


**Fig. 3.** Time evolutions of the normalized background potential energy  $BPE^*$  from experiments with  $\Delta x = 1.25$  m and  $Re_H = 10^3$  and  $10^4$ . The curves from the reference LES ( $Re = 10^3$ ) and LES ( $Re = 10^4$ ) experiments are also shown for comparison. Note the overlap between curves from experiments  $le-1.25-ke-10^3$  and  $le-1.25-ctrl-10^3$ ; and  $le-1.25-ke-10^4$ ,  $le-1.25-kpp-10^4$  and  $le-1.25-ctrl-10^4$ .

In cases with  $Re_H = 10^3$ , mixing from ROMS as quantified by  $BPE^*$  is found to decrease with finer spatial resolution, as follows: the cases with 10 m resolution significantly overestimate mixing and the results are greatly improved when the resolution is increased to 5 m (although mixing is still overestimated); those with 2.5 m resolution give the most accurate results; and those with 1.25 m resolution lead to an underestimation of mixing with respect to the LES curve (Fig. 2). Thus, no convergence of results is achieved, as the mixing curves from ROMS keep changing with spatial resolution. Also, during the initial stage (when shear-driven mixing dominates), the results are not sensitive to the choice of turbulence closure. However, as the system approaches the internal wave regime, KPP-Ri tends to give somewhat more mixing than  $k-\varepsilon$  at coarser resolutions (10 and 5 m) and less mixing at finer resolutions (2.5 and 1.25 m). Nevertheless, the difference in mixing obtained with these closures is not significant when compared to the difference in mixing obtained when varying the model resolution.

The experiment with 2.5 m resolution and U3H/C4V tracer advection scheme ( $le-2.5-u3h-10^3$ ) shows excessive mixing until about  $t^* \approx 25$  and the  $BPE^*$  then decreases for  $25 \leq t^* \leq 50$ , which is an unphysical behavior (Fig. 2). Fig. 4 shows the probability density function of temperature at four non-dimensional times and for the different tracer advection schemes evaluated here. Initially (at  $t^* = 0$ , not shown), only two temperature values are presented (highlighted by the black lines in Fig. 4(d)) and each correspond to 50% of the total volume. At  $t^* = 0.7$  (Fig. 4(a)), a range of new temperature values have formed as a consequence of mixing and with the U3H/C4V scheme a significant percentage of the total volume falls outside the initial temperature range. There is a large increase in the amount of intermediate temperature values generated during the initial stage, when shear-driven mixing dominates (compare Fig. 4(a) and (b)), and, therefore, the  $BPE^*$  curves increase monotonically regardless of the tracer advection scheme (Fig. 2).

Ilicak et al. (2012) used the lock-exchange case to analyze the spurious dianeutral transport in a suite of ocean models. They

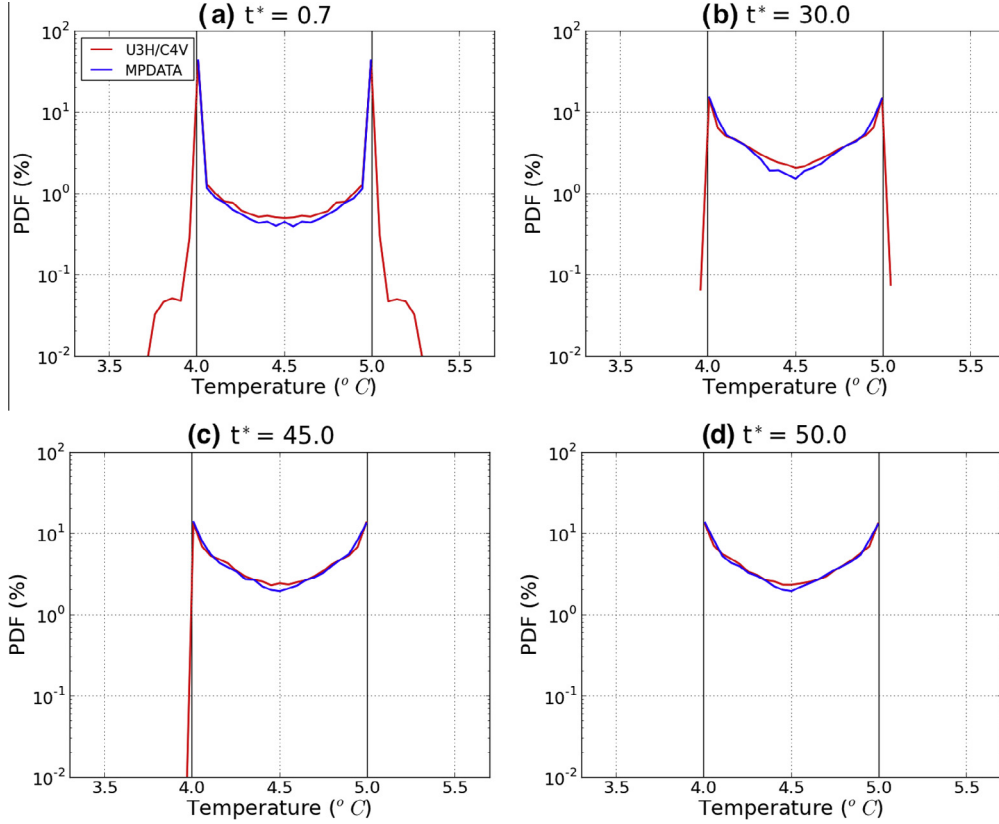


**Fig. 4.** Probability density function (pdf, in %) of temperature ( $^{\circ}$ C) at (a)  $t^*=0.7$ , (b)  $t^*=30.0$ , (c)  $t^*=45.0$  and (d)  $t^*=50.0$  for the different tracer advection schemes evaluated here, namely MPDATA and U3H/C4V (experiments le-2.5-ke- $10^3$  and le-2.5-u3h- $10^3$ , respectively). Animation of the time evolution of the pdf is available in the Auxiliary Materials ([pdf-le-2.5-ke-1000-vs-le-2.5-u3h-1000.mov](#)).

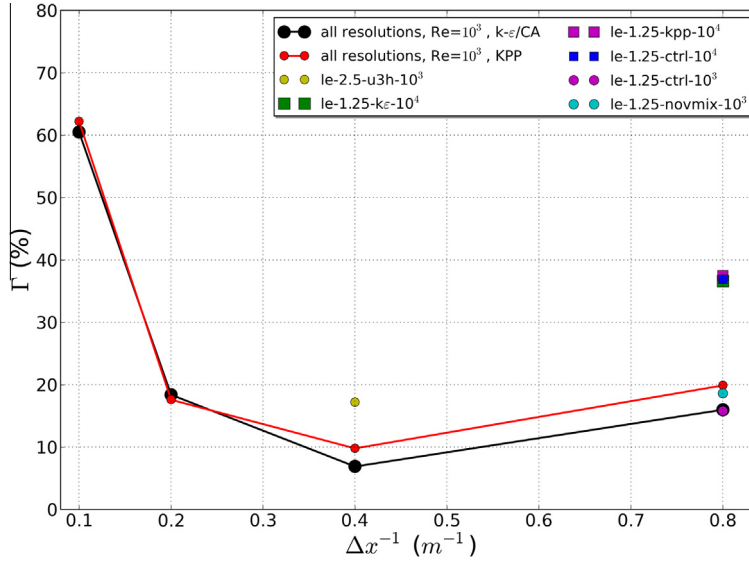


**Fig. 5.** BPE\* normalized root-mean-square errors ( $\Gamma$ , defined by ((13)) see text for details) as a function of the inverse grid resolution ( $\Delta x^{-1}$ ,  $m^{-1}$ ) for all ROMS experiments presented in Table 1. Note the overlap between points from experiments le-1.25-ke- $10^3$  and le-1.25-ctrl- $10^3$ ; le-1.25-ke- $10^4$ , le-1.25-kpp- $10^4$  and le-1.25-ctrl- $10^4$ ; and le-1.25-novmix- $10^3$  and le-1.25-kpp- $10^3$ .

compared the effect of two tracer advection schemes implemented in the MITgcm model (the non-monotonic second order moment scheme of Prather (1986); and a monotonic 7th-order scheme) and also found that new water masses with densities outside the initial range were generated when using the scheme without a flux limiter (Prather). They also highlighted that the noisy vertical

velocity (due to the strong lateral flow divergence) can lead to a nontrivial degree of flux limiting introduced by the monotonic scheme, which would result in large spurious mixing. Here, on the other hand, we found that the monotonic scheme (MPDATA) gives less mixing when compared to U3H/C4V. We present two plausible hypotheses for this behavior. First, the amount of diffu-

sion introduced by the velocity dependent hyper-viscosity from the tracer advection scheme U3H may overcome the effect of the flux limiting on mixing due to the noisy vertical velocity. Since the solutions become smoother as the collapse of turbulence to internal waves takes place, this could explain the decrease in BPE for U3H/C4V scheme at later times. A second hypothesis takes in consideration the fact that the over- and under-shootings observed at the initial stages (Fig. 4(a) and (b)) are not included in the BPE calculation (see Section 3.2). The decrease in the BPE for the U3H/C4V scheme at later times may then, in fact, be due to a reduced impact of the over- and under-shootings (Fig. 4(c) and (d)), rather than some kind of “unmixing” or numerical artifact. Clearly both hypotheses require further investigation, which is beyond the scope of this article.

In the case with  $Re_H = 10^4$ , results from 1.25 m resolution ROMS computations seem to lead to large errors, independently from the closures used (Fig. 3). The LES results show a clear increase in mixing as  $Re$  is increased while in ROMS such growth is not very pronounced. The spatial resolution of 1.25 m does not allow us to keep the implicit numerical diffusion smaller than  $K_{MH} = 1.12 \times 10^{-3} \text{ m}^2 \text{ s}^{-1}$ , which leads to an unintended increase in the effective  $Re_H$  of the system. Clearly, one may also opt to go with coarser resolution and obtain higher mixing by numerical effects. Nevertheless, this cannot be considered as a systematic and reliable modeling approach to turbulent mixing problems.

To better quantify the difference between the BPE\* curves derived from ROMS and LES, we compute the normalized root-mean-square error ( $\Gamma$ ) defined as

$$\Gamma = \frac{\sqrt{\frac{1}{n} \sum_{i=0}^n (\hat{\theta}_i - \theta_i)^2}}{\hat{\theta}_{\max} - \hat{\theta}_{\min}}, \quad (13)$$

where  $\hat{\theta}$  and  $\theta$  are the BPE\* values for the LES and ROMS, respectively, and  $n$  is the number of points compared. The values of  $\Gamma$  as a function of the inverse grid resolution (wave-number) are presented in Fig. 5. Each experiment is compared with the respective LES ( $Re = 10^3$  and  $10^4$ ) based on their  $Re_H$  value.

From Figs. 2, 3, 5, it is clear that the best results are achieved with experiments le-2.5-ke- $10^3$  and le-2.5-kpp- $10^3$  ( $\Gamma = 6.9$  and 8.7%, respectively). The coarser resolution cases, le-10-ke- $10^3$  and le-10-kpp- $10^3$  ( $\Gamma = 60.5$  and 62.5%, respectively) and le-5-ke- $10^3$  and le-5-kpp- $10^3$  ( $\Gamma = 18.4$  and 19.6%, respectively), overestimate mixing, while the higher resolution cases le-1.25-ke- $10^3$  and le-1.25-kpp- $10^3$  ( $\Gamma = 16.0$  and 18.7%, respectively) underestimate it. Experiments using different turbulence closures and  $Re_H = 10^3$  do not show a significant difference in mixing relative to the difference obtained using different modeling choices. Therefore, the choice of turbulence closure plays a minor role in this problem. Experiments carried at higher  $Re_H$  ( $10^4$ ) show that mixing is underestimated with respect to the reference results, with errors increasing by a factor of approximately 2 (le-1.25-ke- $10^4$  ≈ le-2.5-kpp- $10^4$  ≈ le-2.5-ctrl- $10^4$ ,  $\Gamma \approx 37.0\%$ ) compared to cases where  $Re_H = 10^3$ . This is expected since the implicit numerical diffusion associated with the horizontal advection scheme does not allow the effective  $Re_H$  to be increased to  $10^4$  at this resolution. We highlight that there are no significant differences between experiments le-1.25-ke- $10^4$ , le-2.5-kpp- $10^4$ , le-2.5-ctrl- $10^4$ , suggesting that, when the specified  $Re_H$  is large, the implicit horizontal numerical diffusion is more influential than the choice of turbulence closure used.

Results from experiment le-2.5-u3h- $10^3$  show that mixing is significantly changed when the tracer advection scheme formed by U3H/C4V is applied ( $\Gamma = 17.2\%$ , compared to 6.9% achieved using MPDATA). The overall (all resolutions) change in  $\Gamma$  due to different vertical turbulence closures is  $\sim 2\%$ , while the difference in  $\Gamma$  due to different tracer advection schemes is of 10.3%. The error obtained with U3H/C4V is equivalent to those achieved with a

coarser grid resolution ( $\Delta x = 5 \text{ m}$ ) and, therefore, this is considered excessive mixing. It should be noted, however, that the combination formed by U3H/C4V is significantly cheaper in terms of computation time than MPDATA (Table 2). Additional combinations (not shown) formed by U3H and a splines vertical scheme (U3H/Splines) also result in excessive mixing ( $\Gamma = 16.2\%$ ). Even larger mixing is achieved when using the ROMS default fourth-order centered for both horizontal and vertical schemes (C4H/C4V,  $\Gamma = 37.6\%$ ); and a fourth-order centered as the horizontal scheme with a splines vertical scheme (C4H/Splines,  $\Gamma = 37.8\%$ ). All these combinations also show over- and under-shootings in the probability density function of temperature during the initial stage and the lack of monotonicity in the BPE curve at latter times.

The convergence achieved with the different grid resolutions and tracer advection schemes should be interpreted with caution. Resolving the small-scale sharp gradients in the density field during the evolution of the LE problem is a challenging task for any OGCM. The hydrostatic approximation breaks down when the condition  $Fr^2 a^{-2} \ll 1$  does not hold (McWilliams, 1985; Vallis, 2006), which is the case during initial stage of the LE problem. This causes an inverse dependence of the vertical velocity on the grid resolution (Fringer et al., 2006; Ilicak et al., 2012). Under such conditions, one cannot expect the solutions to converge following the order of the numerical scheme, as is the case for classical convergence analysis, and the common idea that higher spatial resolution yields better results does not apply. Therefore, it is not possible to find a scaling to predict the optimal resolution *a priori* and the best modeling choices will vary for each particular case.

## 4. Upper ocean frontal instability for lateral stirring

### 4.1. Model configuration and parameters

In the MLI problem we use the Nek5000 results described in Özgökmen et al. (2011). The non-dimensional parameters in (1) were set to  $a = 20$ ,  $Fr = 0.1$ ,  $Ro = 0.02$ ,  $Re = 10^5$  and  $Pr = 7$ , and the reader is referred to Özgökmen et al. (2011) for further details on the Nek5000 configuration.

In ROMS, the model parameters and the physical conditions are set as close as possible to those in Nek5000. We use a simple rectangular box (Fig. 6), where the domain length is taken equal to its width ( $L = W = 10,000 \text{ m}$ ) and the total water depth set consistent to the depth of a main thermocline ( $H = 500 \text{ m}$ ). For this particular MLI study, the choice of tracer advection scheme is not critical. We conducted simulations (not shown) using U3H/C4V, MPDATA and U3H/Splines and no significant differences were observed in the results. Therefore, we chose to use the same scheme for both momentum and tracer and performed all the MLI simulations using U3H/C4V. The boundary conditions are periodic in the  $x$  direction and free-slip, closed wall, in the  $y$  direction.

The initial condition is:

$$\rho'(\mathbf{x}, 0) = \left[ 1 - 0.7 \times \left( 1 - \frac{z}{H} \right)^{2.3} \right] \left[ 1 - \exp \left\{ - \left( \frac{y/L}{\lambda} \right)^4 - \left( \frac{z}{0.2} \right)^8 \right\} \right] / 98, \quad (14)$$

where

$$\begin{aligned} \lambda &= 0.5 + 0.05 \cos \left( 2\pi \frac{x}{L} \right) + 0.006 \cos \left( 2\pi \frac{x}{L/5} \right) \\ &\quad + 0.003 \cos \left( 2\pi \frac{x}{L/25} \right) \end{aligned} \quad (15)$$

This profile represents a  $h_0 \approx 80 \text{ m}$  deep mixed-layer and an approximately 3 km wide front resting on a stably-stratified fluid (Fig. 6 bottom). This initial condition is similar to that in Özgökmen et al. (2011), but since ROMS uses dimensional

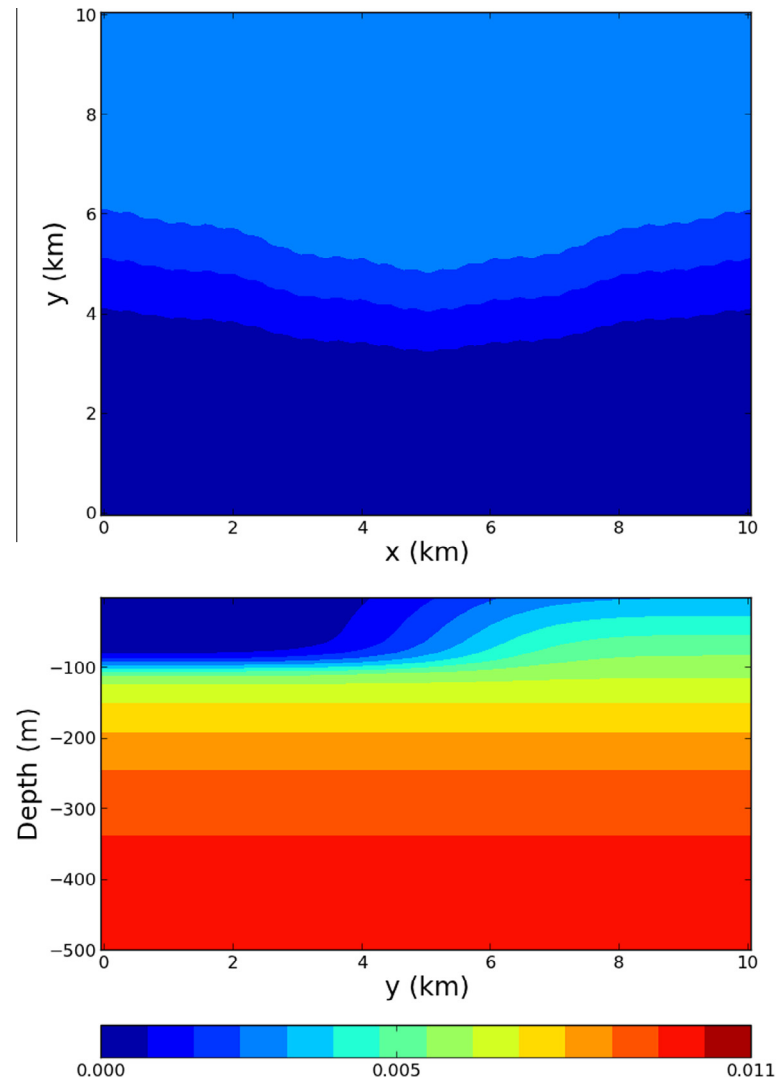


**Fig. 6.** Initial condition for the MLI density perturbation field  $\rho'(\mathbf{x}, t = 0)$  ( $\text{kg m}^{-3}$ ), (top) surface horizontal section and (bottom) vertical cross section.

variables, it has been scaled by 98 to keep the parameters described in the following section consistent with those from Nek5000. In addition, two smaller sinusoidal perturbations in (15) are included to facilitate the development of the desired instabilities. In the absence of these perturbations, the development of instabilities is delayed by several days. The initial temperature condition is set by using the linear equation of state defined in (7) and the initial density perturbation field  $\rho'(\mathbf{x}, 0)$ , given in (14). The integrations start from rest and contain no forcing. Following Öztökmen et al. (2011), wind forcing is neglected for reasons of dynamical simplicity and to limit the parameter space.

From Fig. 6, the resultant buoyancy frequency is  $N \approx 4.42 \times 10^{-4} \text{ s}^{-1}$ . One of the challenges here is to estimate the flow speed scale ( $U_0$ ) that arises from the density field. From the numerical model results presented here, the maximum flow speed 4 h after initialization is  $U_0 \approx 0.02 \text{ m s}^{-1}$ , which gives  $Fr = U_0/(NH) \approx 0.1$ . We set the Coriolis parameter as  $f = 1.21 \times 10^{-4} \text{ s}^{-1}$ , giving  $Ro = U_0/(fL) \approx 0.02$ .

For this MLI problem, the ratio between the fastest growing modes  $R$  and the mixed-layer radius of deformation  $R_d = \sqrt{\frac{g}{\rho_0} \Delta \rho'_m h_0}/f$  (where  $\Delta \rho'_m$  is the density difference across the surface front), over a wide regime of parameters, falls in a narrow range of  $4 \leq R/R_d \leq 6$  (Eldevik and Dysthe, 2002). Following Öztökmen et al. (2011), we assume  $R/R_d \approx 5$ . From Fig. 6,

$\Delta \rho'_m \approx 3.1 \times 10^{-3}$ , and we get  $R_d \approx 400 \text{ m}$ . Thus, the size of the horizontal mixing layer eddies is  $R \approx 2 \text{ km}$ . These parameters are consistent with the  $Fr = 0.1$  simulation presented by Öztökmen et al. (2011).

Three numbers of vertical levels ( $N_\sigma = 16, 32$  and  $64$ ) are used and in all cases the vertical S-coordinate is configured using (following the ROMS terminology): Vtransform = 1 (transformation equation); Vstretching = 1 (stretching function); theta\_s = 7 (surface stretching parameter); theta\_b = 0.1 (bottom stretching parameter); and cline = 100 (critical depth, m). This configuration gives higher vertical resolution near the surface to better resolve the MLI's (Fig. 7).

Unlike in the LE case, in which stratified overturning and turbulent interactions play a key role in the overall mixing in the system, here our interest is on the turbulent exchange across the front by resolved MLI eddies.

#### 4.2. Experimental description and tracer metrics

Table 3 presents the main parameters for the seven numerical experiments conducted in the MLI study. The simulation names are specified using the following logic (e.g., mli-100-32-ke): type of problem – horizontal resolution (m) – number of vertical layers – turbulence closure or absence of vertical mixing (novmix).

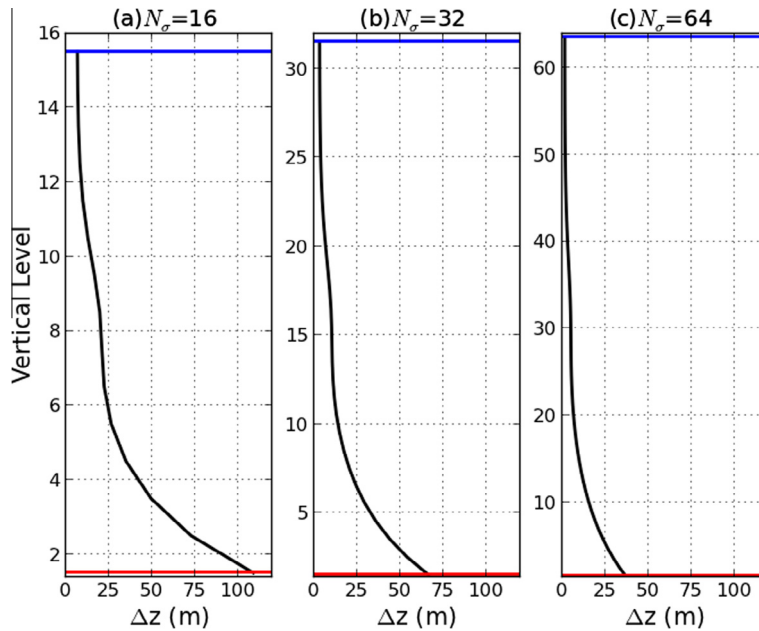


**Fig. 7.** Layer thickness ( $\Delta z$ , m) as a function of vertical level for (a)  $N_\sigma = 16$ , (b)  $N_\sigma = 32$  and (c)  $N_\sigma = 64$ . The blue and red lines represent the surface and bottom layers, respectively. (For interpretation of the references to colour in this figure legend, the reader is referred to the web version of this article.)

**Table 3**

List of MLI experiments conducted, where  $N_\sigma$  is the number of sigma levels,  $\Delta x = \Delta y$  is the horizontal grid spacing and CA = Canuto-A stability function. The minimum and maximum vertical grid spacing ( $\Delta z$ ) values are also shown.

| Exp.              | $\Delta x = \Delta y$ (m) | $N_\sigma$ | min/max $\Delta z$ (m) | Turb. closure |
|-------------------|---------------------------|------------|------------------------|---------------|
| mli-100-32-kε     | 100                       | 32         | 3.3/73.9               | k-ε/CA        |
| mli-200-32-kε     | 200                       | 32         | 3.3/73.9               | k-ε/CA        |
| mli-50-32-kε      | 50                        | 32         | 3.3/73.9               | k-ε/CA        |
| mli-100-16-kε     | 100                       | 16         | 6.6/133.9              | k-ε/CA        |
| mli-100-64-kε     | 100                       | 64         | 1.6/38.9               | k-ε/CA        |
| mli-100-32-kpp    | 100                       | 32         | 3.3/73.9               | KPP-Ri        |
| mli-100-32-novmix | 100                       | 32         | 3.3/73.9               | none          |

In these experiments we vary horizontal and vertical resolutions, as well as apply the same turbulent closures presented in Section 3.2 (k-ε/CA and KPP-Ri). It should be noticed that the Richardson number-dependent KPP is designed to parameterize ocean mixing below the boundary layer (Large et al., 1994). Since there is no external forcing in our MLI experiments, the purpose of using KPP-Ri is to evaluate how the system evolves during, for example, the spin-down of a mixed-layer front created by the passage of a storm. The vertical background diffusivity ( $K_{CV}^0$ ) is set to the  $5.0 \times 10^{-3}$  m $^2$  s $^{-1}$ , which is the value recommended by Large et al. (1994) based on the observed diffusivities reported for the seasonal thermocline (Peters et al., 1988). The vertical background viscosity ( $K_{MV}^0$ ) is set to  $3.5 \times 10^{-2}$  m $^2$  s $^{-1}$ . In addition, we carry out a control experiment (mli-100-32-novmix), where both  $K_{CV}$  and  $K_{MV}$  are set to zero. These are some of the modeling choices that are faced during the implementation of an OGCM and, therefore, the outcomes will provide some guidance for applications focusing on the lateral dispersion of pollutants and biogeochemical tracers due to submesoscale MLI eddies.

The baroclinic time step is set to  $\Delta x/5$  s and the number of barotropic time steps between each baroclinic time step is set to 20. This yields a maximum lateral CFL number of  $9.9 \times 10^{-1}$  for all simulations. The approximate wall clock time as well as the number of nodes for each MLI experiment for an integration time of 30 days are summarized in Table 2.

One of the purposes of this study is to quantify the transport and mixing of a passive tracer field  $C(\mathbf{x})$  during the mixing layer adjustment. In ROMS, such a tracer field evolves in time following (6), where the horizontal and vertical diffusion coefficients are the same as those for temperature ( $K_{CH}$  and  $K_{CV}$ , respectively). The initial concentration of  $C(\mathbf{x})$  is specified as:

$$C_0(\mathbf{x}) = \exp\left(-\frac{(y - y_c)^2}{l_y^2}\right) \exp\left(-\frac{z^2}{l_z^2}\right), \quad (16)$$

where  $y_c = 10,000$  m is at the center of the domain,  $l_y = 500$  m and  $l_z = 100$  m. A three-dimensional view of the initial concentration field  $C_0(\mathbf{x})$  is shown in Fig. 8. Although a release of this size might not be feasible in a field experiment, it ensures the tracer is well resolved in all the horizontal and vertical resolutions used in our numerical experiments. Using a more experimentally practical release could introduce numerical artifacts, since the initial patch of tracer would be near the limits of the model resolution. In all experiments presented here, the tracer is released 15 days after the beginning of the simulation, when the flow is fully non-linear (Fig. 9(b)).

To quantify the net turbulent expansion of the front by ML eddies, we compute the second moment (or tracer variance) of the tracer concentration field across the front and at a fixed level of  $z_0 \approx 5$  m,

$$\sigma_y^2(t, z_0) = \frac{M_{02}(t, z_0) - M_{01}^2(t, z_0)}{M_{00}(t, z_0)}, \quad (17)$$

where

$$M_{mp}(t, z_0) = \frac{1}{A} \iint x^m y^p C(x, y, z_0, t) dx dy. \quad (18)$$

The tracer variance is frequently employed in the analysis of observational data (Sundermeyer and Ledwell, 2001; Inall et al., 2013).

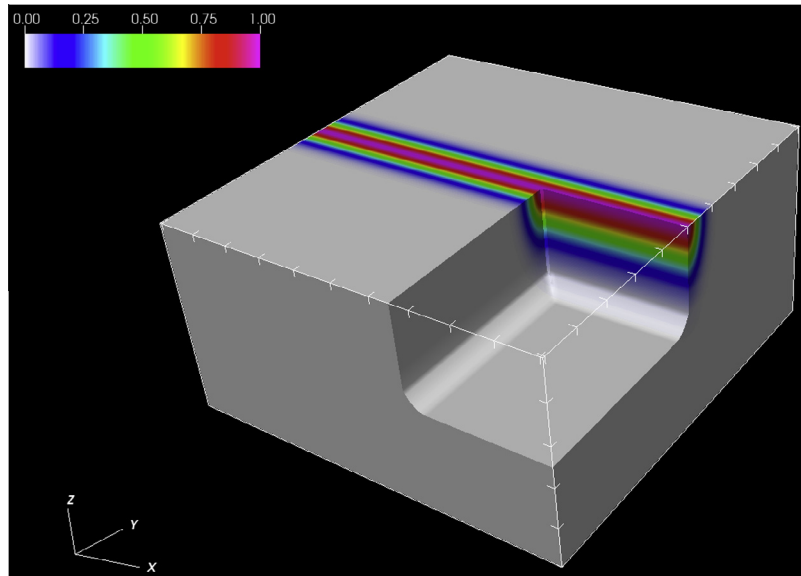


**Fig. 8.** Three-dimensional view for the initial tracer concentration field  $C_0(\mathbf{x})$ . The color bar shows concentration in  $\text{kg m}^{-3}$ . Tick marks are placed every 1 km in the horizontal and 100 m in the vertical directions. Animation of the time evolution of  $C(\mathbf{x})$  for experiment mli-100-32A-dye is available in the Auxiliary Materials ([mli-res100-32A-dye.mov](#)). (For interpretation of the references to colour in this figure legend, the reader is referred to the web version of this article.)

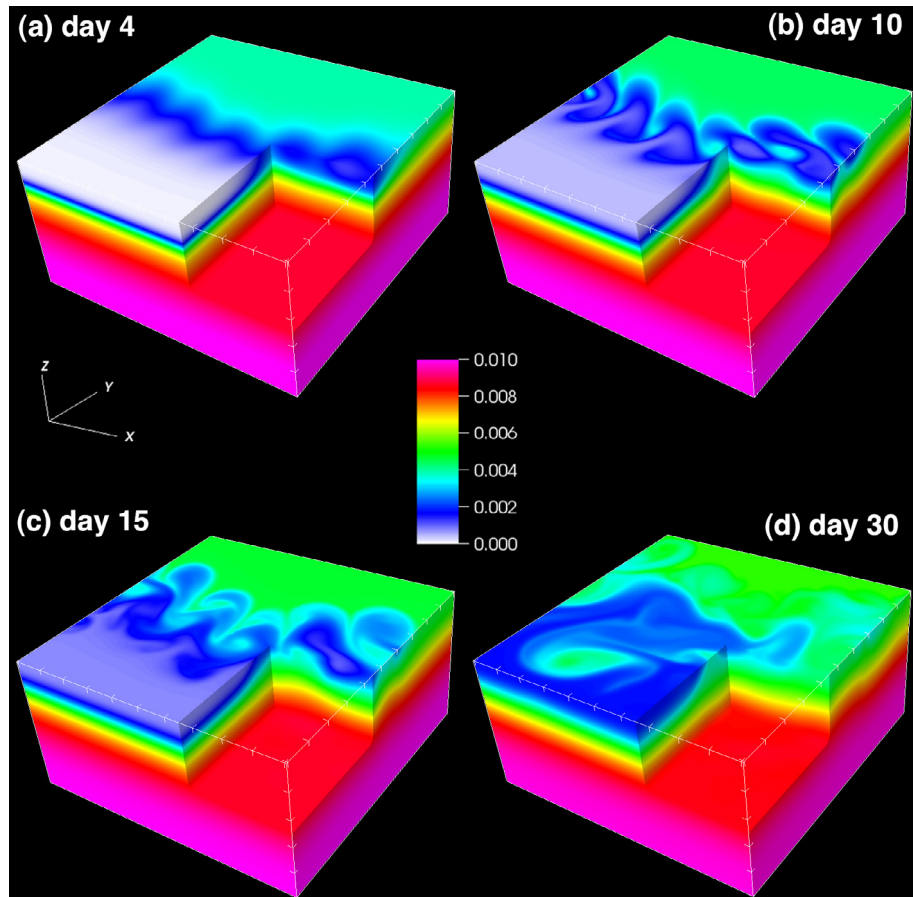


**Fig. 9.** Density perturbation field  $\rho'$  ( $\text{kg m}^{-3}$ ) for experiment mli-res100-32A at (a)  $t = 4$  days, (b)  $t = 10$  days, (c)  $t = 15$  days and (d)  $t = 30$  days. The thick marks are placed every 1 km in the horizontal and 100 m in the vertical. Corresponding animation is available in the Auxiliary Materials ([mli-res100-32A-rho.mov](#)).

#### 4.3. Description of the flow

**Fig. 9** presents snapshots of the 3D density perturbation field  $\rho'$  for experiment mli-100-32- $k\epsilon$  (see **Table 3**) at four different times. Initially (right after  $t = 0$  days, not shown), inertial oscillations are created, where the vertical isopycnals start to oscillate around the geostrophically adjusted state, consistent with predictions by Tandon and Garrett (1994). As pointed by Boccaletti et al. (2007), there are no significant changes in stratification during this period. After a few days, MLLs are visible and restratification begins (**Fig. 9(a)**). After ten days (**Fig. 9(b)**), the presence of coherent vortices with scales consistent with  $R \approx 2$  km are clearly observed. Once the instability becomes fully nonlinear (**Fig. 9(c)**), the 3D density perturbation field is visually very similar to the LES simulation by Öztürk et al. (2011) (see their **Fig. 2(b)**). At day 30 (**Fig. 9(d)**), the exchange flow associated with restratification gets close to the domain boundaries. Since the boundary induced shears and flows become important beyond this stage (not shown), we finalize the integration.

#### 4.4. Comparison of lateral stirring from LES and ROMS

We now focus on the transport and stirring of a passive tracer field during the MLI adjustment process. In particular, we compute near surface wave-number spectra and the time evolution of the second moment of the tracer distribution.

To quantify the difference in tracer evolution from the experiments listed in **Table 3**, horizontal wave-number spectra of the near surface ( $\approx 5$  m) tracer fields are shown in **Fig. 10**. These are computed by averaging over 20 one-dimensional spectra taken along the periodic direction  $4 \text{ km} \leq y \leq 6 \text{ km}$  at 3 and 6 days after the initial tracer release. At scales comparable to the mixing layer eddies ( $k \approx 5 \times 10^{-4} \text{ m}^{-1}$ ), most of the energy shown in the LES curve is well captured by the experiments with  $\Delta x = 50$  m. The ROMS spectra do not change significantly when either  $N_\sigma$  varies or the turbulence closure is changed (the spectra from experiments mli-100-32- $k\epsilon$ , mli-100-16- $k\epsilon$  and mli-100-64- $k\epsilon$ ; and from experiments mli-100-32-kpp and mli-100-32-novmix are very similar). In tracer stirring carried out by approximately two-dimensional

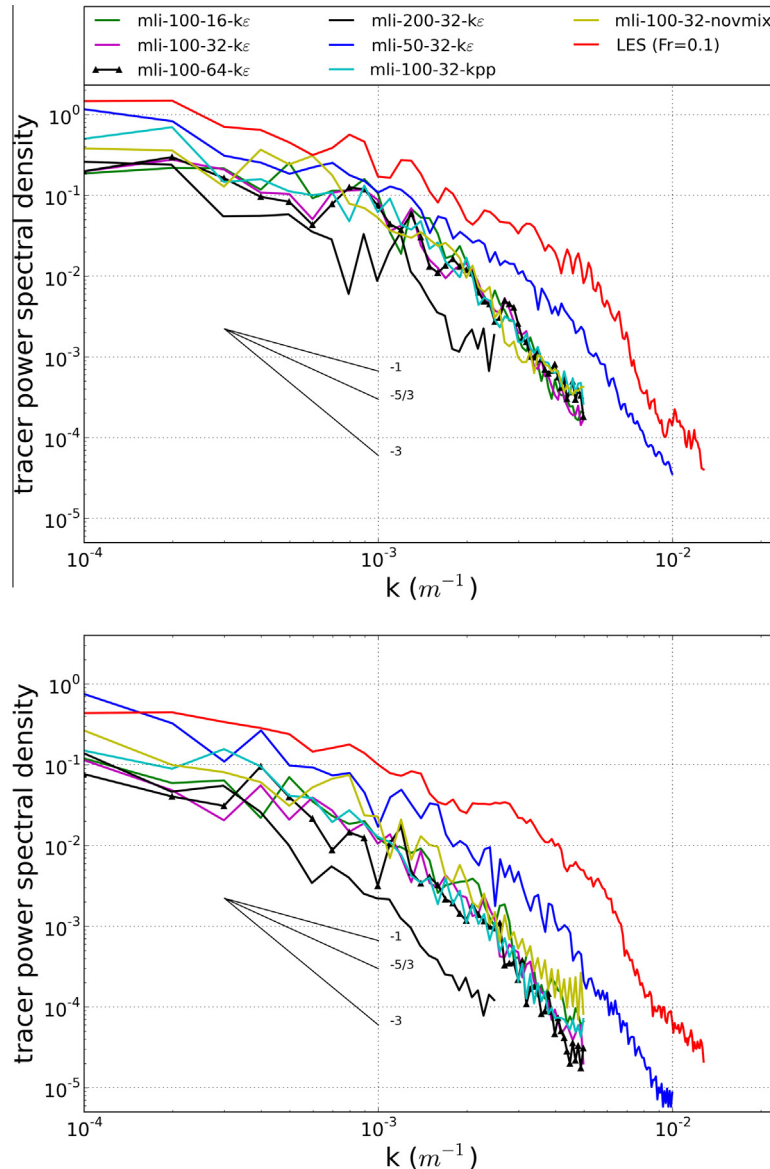


**Fig. 10.** Tracer wave-number power spectral densities for experiments listed in **Table 3** at (top) time = 18 days and (bottom) time = 21 days. The LES ( $Fr = 0.1$ ) results by Öztürk et al. (2009b) at corresponding times are also superimposed for comparison. Note the similarity between the spectra from experiments mli-100-32- $k\epsilon$ , mli-100-16- $k\epsilon$  and mli-100-64- $k\epsilon$ ; and experiments mli-100-32-kpp and mli-100-32-novmix. Typical wave-number slopes are shown in the background.

flow features a scaling of  $k^{-1}$  is expected (Vallis, 2006). The ROMS simulations display a more limited range of  $k^{-1}$  scaling, while the LES curves are approximately consistent with this slope down to  $k \approx 5 \times 10^{-2} \text{ m}^{-1}$ . The energy spectrum from the ROMS experiments become more similar to the LES curve as horizontal resolution is increased.

The time evolution of the tracer variances in the near surface are presented in Fig. 11. The results are shown until day 21, since in our control experiment (mli-100-32-novmix) boundary induced shears and flows become important beyond this point (not shown). This metric suggests that the ROMS experiments are not significantly affected, compared to other modeling choices tested here, when either  $N_\sigma$  or  $\Delta x$  are varied. Better agreement with the LES results is obtained using the second order closure model ( $k\cdot\varepsilon/\text{CA}$ ) at all resolutions used. The curve from experiment mli-100-32-kpp resembles again our control run and significant deterioration

of the solution is found in these experiments (see Section 4.5 for more details).

From the curves presented in Fig. 11, the  $y$ -component of diffusivity can be obtained following:

$$K_y = \frac{1}{2} \frac{\partial \sigma_y^2}{\partial t}. \quad (19)$$

We compute  $K_y$  using a 6-h interval and then calculate the normalized root-mean-square error ( $\Gamma$ , defined in Eq. 13) with respect to the LES diffusivity. This interval is arbitrarily chosen and, qualitatively, the results described below are not sensitive to the time interval used (we tested values ranging from 2 to 24 h). In the ROMS experiments, the time-averaged  $y$ -direction horizontal diffusivities ( $K_y$ ) range from 2.1 to  $5.5 \text{ m}^2 \text{ s}^{-1}$ , while for the LES experiment the value is  $2.0 \text{ m}^2 \text{ s}^{-1}$ . These values are all within the limits observed over the continental shelf and below the mixed layer on

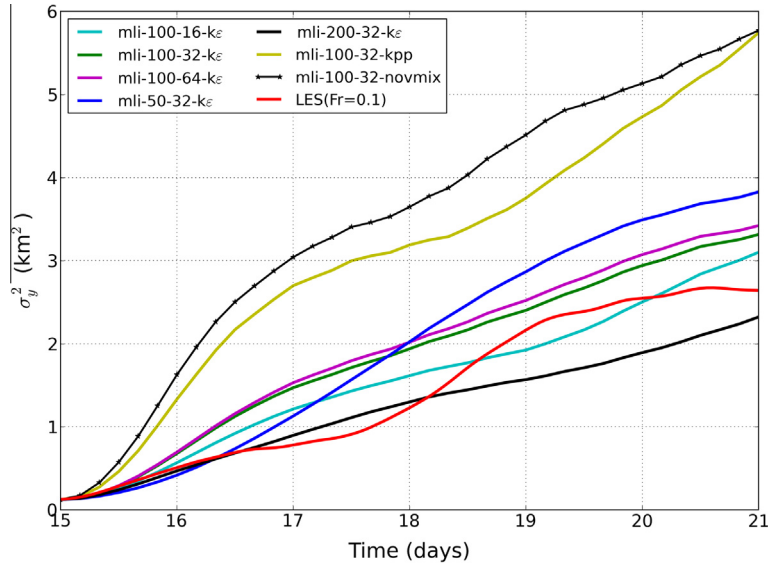


**Fig. 11.** Second moment of the tracer distribution as a function of time for the MLI experiments listed in Table 3. The curves from experiments mli-100-32-kpp and mli-100-32-novmix are very similar. The LES ( $Fr = 0.1$ ) curve presented in Özgökmen et al. (2011) is also superimposed for comparison.

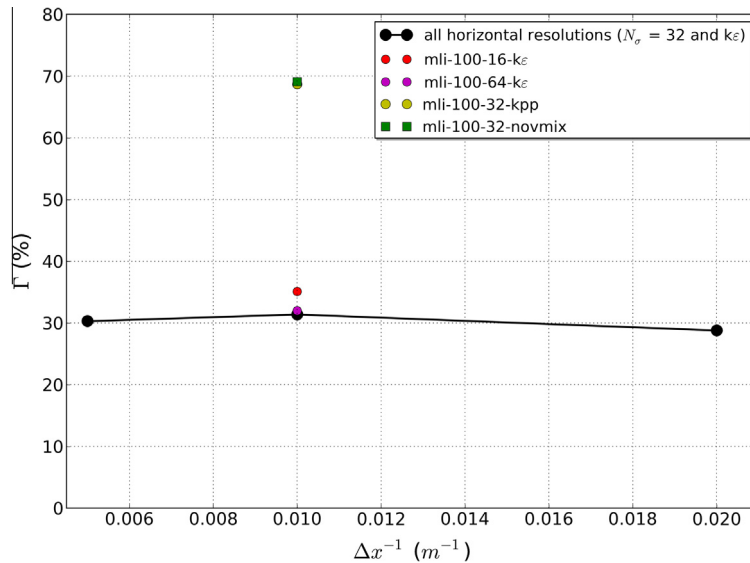


**Fig. 12.** Normalized root-mean-square errors computed from the  $y$ -direction horizontal diffusivities  $\langle K_y \rangle$  ( $\Gamma$ , defined by Eq. (13); see text for details) as a function of the inverse grid resolution ( $\Delta x^{-1}, \text{m}^{-1}$ ) for all MLI experiments presented in Table 3. Note the overlap between points from experiments mli-100-32-kε and mli-100-64-kε; and mli-100-32-kpp and mli-100-32-novmix.

spatial scales of 1–10 km and timescales of less than 5 days (Sundermeyer and Ledwell, 2001; Inall et al., 2013). However, we highlight that in nature the problem is considerably more complex than our idealized case and other processes, such as those associated with external forcing, inertial waves or mean flow, may also influence the lateral dispersion of a dye patch. Therefore, it would be difficult to evaluate our results by relying just on the observations. Fig. 12 shows the values of  $\Gamma$  computed for each ROMS simulation. Again, the results are not significantly sensitive to either  $N_\sigma$  or the  $\Delta x$  values tested here. The error for  $\Delta x = 100$  m is the largest (experiment mli-100-32-k $\varepsilon$ ,  $\Gamma = 31.4\%$ ). A small improvement in the solution is achieved if coarser ( $\Delta x = 200$  m) or higher ( $\Delta x = 50$  m) horizontal resolutions are used (experiments mli-200-32-k $\varepsilon$  and mli-50-32-k $\varepsilon$ ,  $\Gamma = 30.3\%$  and 28.8%, respectively). The result from an additional experiment (not shown) with  $\Delta x = 25$  m also shows a small improvement in the solution ( $\Gamma = 26.1\%$ ), but the increase in computing time (wall clock time is  $\sim 2$  times larger than in experiment mli-50-32-k $\varepsilon$ , see Table 2) does not justify such gain. Additionally, the results do not converge

as the vertical resolution is increased and the best solution is achieved when using an intermediate number of sigma layers ( $N_\sigma = 32$ ). Nonetheless, we highlight that the differences in  $\Gamma$  as horizontal and vertical resolution vary are significantly reduced when compared to those obtained in the LE problem (see Section 3.4). Unlike the latter, the hydrostatic approximation holds for the MLI problem (since  $F^2 a^{-2} \ll 1$ ). However, our results are not sufficient to make a connection between better spatial convergence and the fact that the hydrostatic approximation holds and further studies should be conducted to address this point.

Finally, the largest errors obtained are related to the choice of turbulence closure. The use of KPP-Ri results in a much larger error (mli-100-32-kpp,  $\Gamma = 68.7\%$ ) compared with k- $\varepsilon$ /CA (mli-100-32-k $\varepsilon$ ,  $\Gamma = 31.4\%$ ) when using identical horizontal and vertical resolutions. Similarly, the error in the control experiment (mli-100-32-novmix,  $\Gamma = 69.1\%$ ) is significantly larger, suggesting that the turbulence closure has a significant contribution in the stirring of a passive tracer during the MLI adjustment. This point is explored in more detail in the following section.

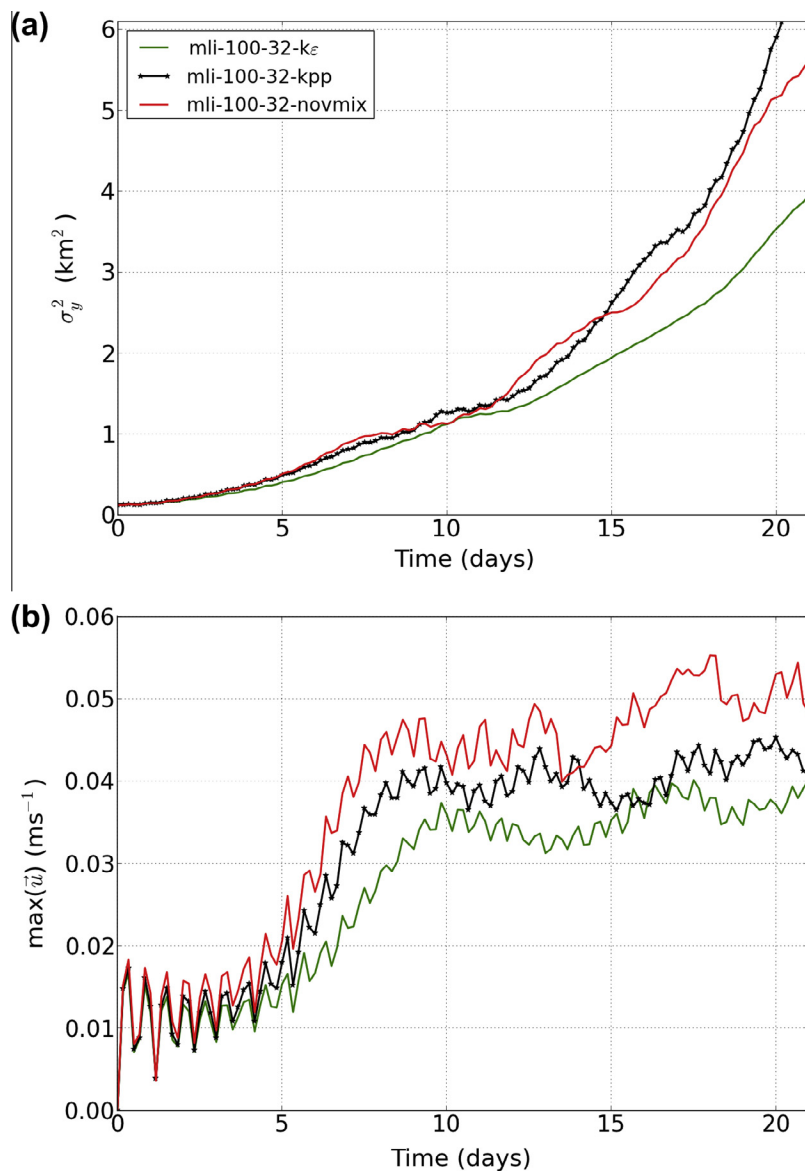


**Fig. 13.** Time series of (a) near surface tracer second moment ( $\sigma_y^2$ , km $^2$ ) and (b) maximum horizontal velocity ( $\vec{u}$ , m s $^{-1}$ ) in the mixed layer. Results from experiments mli-100-32-k $\varepsilon$ , mli-100-32-kpp and mli-100-32-novmix are shown.

#### 4.5. Restratiﬁcation and vertical diffusivity

We now focus on experiments mli-100-32-k $\varepsilon$ , mli-100-32-kpp and mli-100-32-novmix and following Eq. (16) release a passive tracer field at the beginning of the simulation (time = 0 days). The corresponding time evolution of  $\sigma_y^2$  in the near surface are presented in Fig. 13(a). Experiments mli-100-32-kpp and mli-100-32-novmix show larger values of tracer variance throughout the simulation in comparison to mli-100-32-k $\varepsilon$ . The discrepancy is ampliﬁed after day 12. It is instructive to compute a metric for the restratiﬁcation due to the rearrangement of buoyancy by the residual circulation. We compute an overturning eddy streamfunction ( $\psi_e$ ) as follows:

$$\psi_e = \alpha \left( \frac{\alpha \bar{v} \bar{b}' \bar{b}_z - \alpha^{-1} \bar{w} \bar{b}' \bar{b}_y}{\bar{b}_y^2 + \alpha^2 \bar{b}_z^2} \right), \quad (20)$$

where  $b$  is the buoyancy, primes are ﬂuctuations from the mean value (averaged along  $x$  direction and denoted by an overbar) and subscript denotes partial derivatives. This form of  $\psi_e$  (Plumb and Ferrari, 2005; Cerovecki et al., 2009; Mahadevan et al., 2010; Ramachandran et al., 2013) generalizes earlier deﬁnitions and remains well deﬁned in situations where  $\bar{b}_y$  or  $\bar{b}_z$  become negligibly small (e.g., weakly stratiﬁed environments, like the MLI problem applied here). A coordinate stretching parameter  $\alpha = H/L = 0.05$  is used to account for the skewed aspect ratio. Our results are

insensitive to  $\alpha$  over a range  $10^{-2}$ – $10^{-3}$ . The eddy streamfunction always shows a thermally directed circulation, where warm (light) water rises above cold (dense) water. Snapshots of  $\psi_e$  at day 7 are shown in Fig. 14. At this stage, the strength of the secondary circulation is signiﬁcantly larger in experiments mli-100-32-kpp and mli-100-32-novmix when compared to the case with k- $\varepsilon$ /CA. This is because MLI have grown slower in the latter, as shown by the time series of  $\sigma_y^2$  and maximum horizontal velocity within the ML (Fig. 13(a) and (b), respectively). As expected, the discrepancy between experiments with different turbulence closures are due to the values of the explicit vertical diffusivity (and viscosity, not shown), which are zero in our control case and signiﬁcantly larger in the case using k- $\varepsilon$ /CA when compared to the case using KPP-Ri (Fig. 15). We emphasize that the Richardson number-dependent KPP parameterization was not designed to work in the mixed layer and, therefore, it is not surprising that this scheme underestimates the amount of vertical viscosity and diffusivity during the MLI adjustment.

Ramachandran et al. (2013) studied the effect of subgrid-scale mixing in the evolution of the submesoscale instabilities generated in a mixed-layer front forced by downfront winds. Although they did not have a ground truth to compare their results with, they used the eddy kinetic budget to estimate physically meaningful levels for the SGS dissipation under quasi-equilibrium (restratiﬁcation versus destratiﬁcation) conditions. They found non-trivial variability in the amount of dissipation when varying the vertical

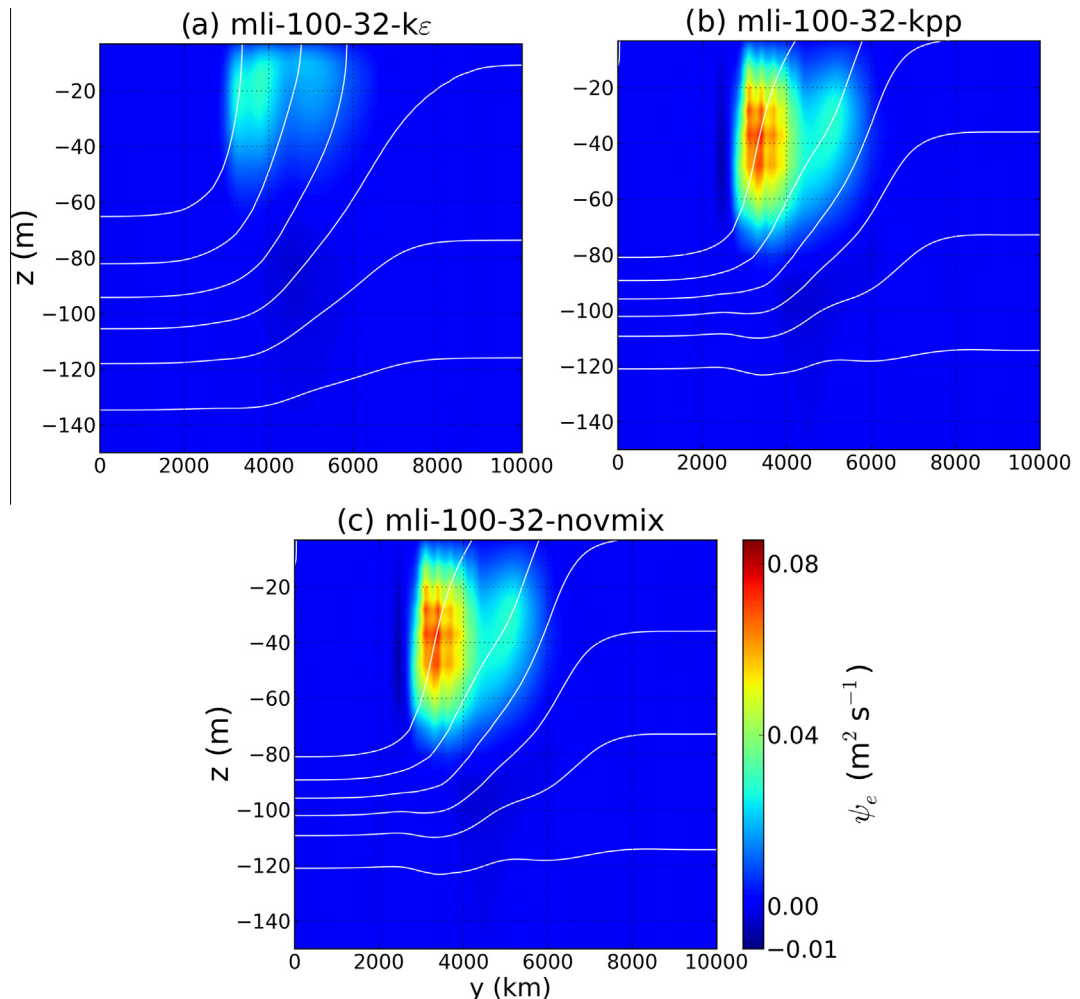


**Fig. 14.** Eddy streamfunction ( $\psi_e$ ,  $m^2 s^{-1}$ ) at day 7 for experiments (a) mli-100-32-k $\varepsilon$ , (b) mli-100-32-kpp and (c) mli-100-32-novmix. White lines show buoyancy contours.

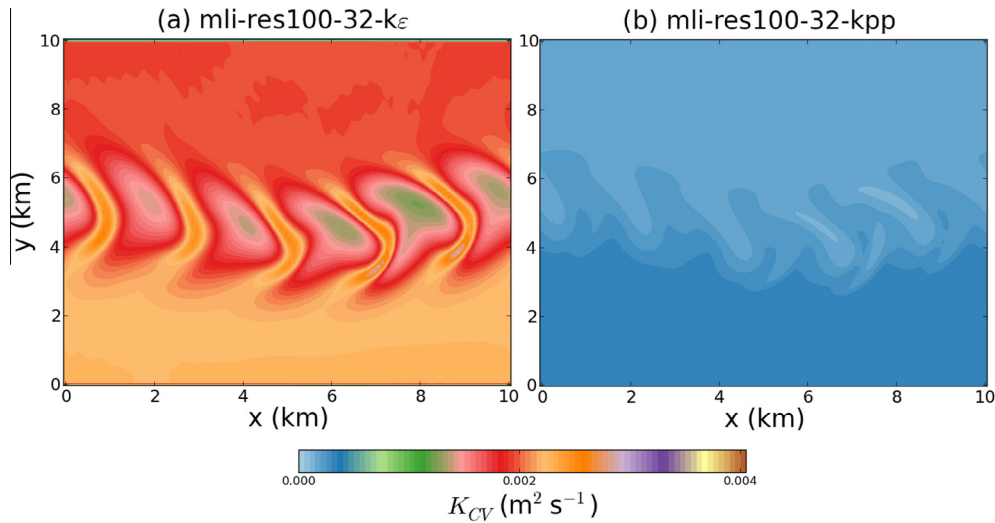


**Fig. 15.** Snapshots of vertical diffusivities ( $K_{cv}$ ,  $m^2 s^{-1}$ ) at  $\sim 40$  m depth after 7 days of simulations from runs using (a) the second order turbulence closure  $k\text{-}\varepsilon$ /CA (experiment mli-100-32- $k\varepsilon$ ) and (b) the algebraic Richardson number based KPP (experiment mli-100-32-kpp).

viscosity in the simulations (while keeping the lateral viscosity constant) and pointed out the need to explore the sensitivity of submesoscale-resolving simulations to the vertical SGS parameterization. Here this sensitivity has been explored and we highlight the importance of adopting a turbulence closure that is able to provide (even in the absence of external forcing) additional viscosity/diffusivity in the mixed-layer, where entrainment is critical.

## 5. Summary and conclusions

This study is motivated by some of the questions that every modeler faces when setting up a problem: what are the most appropriate resolutions, parameters, numerical schemes and turbulence models and how do they affect the solution space? Preferably, such studies should involve oceanic data sets for direct relevance. Nevertheless, in problems involving mixing and stirring, ocean observations can be sparse or incorporate aliasing errors due to the time needed for sampling. In addition, the forcing fields that influence the solution might not always be available. There are many examples of studies that have conducted a direct comparison of numerical solutions with observations (Özgökmen et al., 2003; Xu et al., 2006; Ilıcak et al., 2008, 2009; Chang et al., 2008), and in all of which the precision of comparison was effectively limited by the extent of the observational data set.

Two numerical approaches, LES and OGCM, have recently started to address similar problems in oceanography (i.e., submesoscale motions due to mixed layer instabilities). The LES approach has the full non-hydrostatic dynamics and a more complete way of capturing mixing and stirring (at the expense of computational time), while OGCMs have the full range of functionalities that make the results directly relevant for oceanic applications. However, the LES approach is usually limited in terms of realistic forcing and boundary conditions that drive the flow, whilst in OGCMs mixing and stirring are usually dependent on parameterizations. As such, a clear avenue for gaining more insight into the accuracy of OGCMs solutions for mixing and stirring problems is using LES as reference, provided that idealized yet oceanographically-relevant problems can be set up.

In this study a series of numerical simulations were conducted for two idealized cases, namely the lock-exchange (LE) and the mixed-layer instability (MLI) problems. Our main goal is to compare mixing and stirring derived from two modeling approaches: an OGCM (ROMS) that solves the hydrostatic primitive equations,

and a spectral element model (Nek5000) that integrates the non-hydrostatic Boussinesq equations. Although comparing these two different modeling approaches is not a trivial task, given that the former is configured in terms of dimensional variables while non-dimensional variables are used in the latter, it is a valuable way of testing the accuracy of OGCMs when the scales fall below the mesoscale regime. ROMS is a hydrostatic ocean model formulated in a terrain-following vertical coordinate. Therefore, the results presented here should be fairly applicable to other OGCMs that follow these characteristics. In addition, the results related to the choice of turbulence closure can be generalized to other OGCMs that contain the closures tested here.

In the first part of the paper we apply the LE problem to compare the temporal evolution of mixing under various OGCM modeling choices. As a metric we use the background potential energy (BPE), which quantifies mixing in an enclosed system (Winters et al., 1995). The numerical experiments are configured as similarly as possible to the LES settings, which is used as reference. We explore the effects of various modeling parameters and find that, for a fixed horizontal Reynolds number ( $Re_H = 10^3$ ), mixing is most sensitive to the choice of grid resolution. We show that the choice of turbulence closure plays a minor role in the temporal evolution of mixing for the LE problem. No convergence towards the ground truth reference (LES) is attained as the grid resolution is refined and the best results are achieved using an intermediate spatial resolution (2.5 m). Mixing is underestimated when using a higher grid resolution (1.25 m) and it is overestimated when using coarser grid resolutions (5 and 10 m). Mixing is also better represented at lower  $Re_H$  ( $10^3$ ), since even with our finest grid resolution ( $\Delta x = 1.25$  m) the implicit numerical diffusion associated with the advection scheme does not allow the effective  $Re_H$  to be increased to  $10^4$ . The choice of tracer advection scheme also has an important influence on the mixing. Our results show that the combination formed by U3H/C4V schemes results in excessive mixing (and lack of monotonicity in the BPE), with larger deviation from the LES results when compared to MPDATA. We show the importance of using a monotonic scheme in numerical studies dealing with small-scale stratified mixing, where the initial tracer extrema must be preserved (i.e., overflows and biogeochemical studies). It should be emphasized that a correct representation of the LE problem is a challenging task for any advection scheme available in OGCMs, since it includes sharp gradients in the velocity and density fields as well as non-hydrostatic dynamics. Therefore, one cannot expect

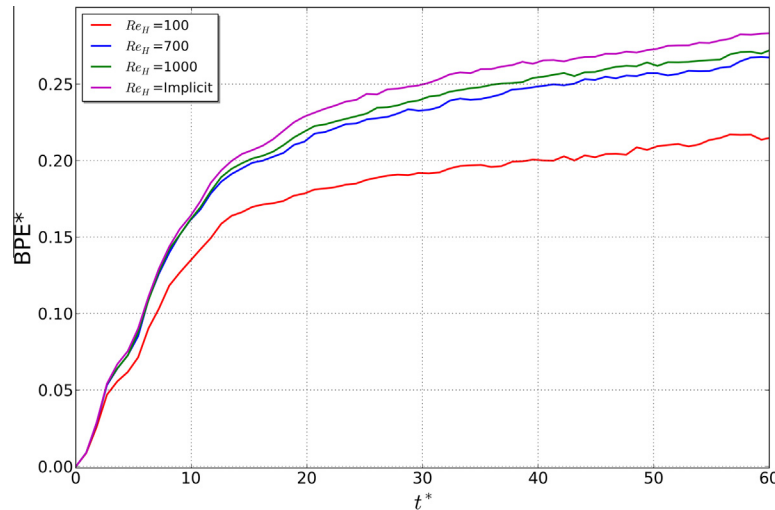


**Fig. 16.** Time evolutions of the normalized background potential energy  $BPE^*$  from ROMS experiments with 10 m resolution and different explicit horizontal Reynolds number ( $Re_H$ ) values.

the solutions to converge following the order of the numerical scheme, as is the case for classical convergence analysis for smooth solutions. Given that the results are largely influenced by the errors associated with the numerical schemes, it is not possible to find a scaling to predict an optimal resolution *a priori*.

The sensitivity of the transport and stirring of a passive tracer field is then studied within the context of the MLI problem. Our simulations are configured as similarly as possible to the LES ( $Fr = 0.1$  case) presented by Özgökmen et al. (2011), which is treated as our ground truth. As a metric, we compute near surface tracer energy spectra and the time evolution of the second moment (or tracer variance), from which the cross-frontal diffusivity is obtained. A total of seven numerical experiments are carried out, where common modeling choices related to horizontal/vertical resolutions as well as turbulence closure are explored. The results do not converge towards the ground truth reference (LES) as the horizontal and vertical grid resolutions are refined. The best solution is achieved when using an intermediate number of sigma layers ( $N_\sigma = 32$ ) and a horizontal grid resolution of  $\Delta x = 50$  m. However, it is likely that the results have already converged with the coarsest spacial resolution tested here ( $N_\sigma = 32$  and  $\Delta x = 200$  m) and the small differences due to different spatial resolutions are due to numerical artifacts. Varying the amount of vertical viscosity and diffusivity (by selecting different turbulence closures) shows more impact on the stirring of a passive tracer field than any other modeling choice investigated here. The best results with respect to the LES run are achieved with  $k\cdot\varepsilon/CA$  and the deviation increases by a factor of approximately two when KPP-Ri is selected. We show that this discrepancy is due to the low values of vertical viscosity/diffusivity given by KPP-Ri and highlight the importance of adopting a turbulence closure that is able to provide (even in the absence of external forcing) additional viscosity/diffusivity in the mixed-layer, where entrainment is critical.

While ROMS simulations differ from LES in the amount of mixing and tracer stirring, the simulated coherent features appear to be quite similar. In addition, the metrics used for comparison are quite precise and perhaps can only be implemented in a model to model comparison, while they could be too challenging to compute from ocean observations. It is unclear how many of the differences between the models are related to nonhydrostatic effects, as the MLI is still under rotational control and ROMS simulations show considerable variability with different parameterizations. Processes at the next range of scales, namely those between the

rotationally-controlled MLI and three-dimensional stratified turbulence, such as Langmuir turbulence (McWilliams et al., 1997; Hamlington et al., 2014), diurnal convection in the mixed layer and inertia gravity waves are expected to contain significant non-hydrostatic dynamics. These processes will perhaps pose a natural resolution limit to the applicability of hydrostatic dynamics. Given that oceanographic flows generally lie in the domain of multi-scale problems, the most logical choice is for OGCMs to start adopting non-hydrostatic pressure solvers, high-order advection schemes (where the associated numerical diffusion will not act as an implicit closure) and SGS parameterizations that depend explicitly on the resolution of the model. There should also be a much more careful evaluation of the latter. There are certainly several attempts in that direction (e.g., Marshall et al., 1998; Fringer et al., 2006; Kanarska et al., 2007; Piggott et al., 2008), even though the pace of change is still dictated by the computational constraints and sparse observational data sets for accurate evaluation.

## Acknowledgments

We greatly appreciate the support of the Office of Naval Research and National Science Foundation via Grants N00014-09-1-0267 and OCE-0961369, respectively. This research was made possible, in part, by a Grant from BP/The Gulf of Mexico Research Initiative. The LES computations were supported by a grant of computer time from the City University of New York High Performance Computing Center under NSF Grants CNS-0855217 and CNS-0958379. We also thank University of Miami's Center for Computational Science for making available their resources. The authors appreciate many helpful discussions with Prof. Mohamed Iskandarani and Jean M. Mensa during the elaboration of this manuscript. Finally, we would like to thank two anonymous reviewers whose questions and comments led to substantial improvement of this manuscript.

## Appendix A. Estimating the explicit Reynolds number ( $Re_H$ ) based on an asymptotic analysis

In this Appendix we show how the explicit horizontal Reynolds number ( $Re_H$ ) was estimated in the ROMS simulations for the lock-exchange problem. We use an asymptotic analysis, similar to that employed in Dong et al. (2007), to assure that the implicit numerical diffusion associated with the advection operator is smaller

than the prescribed explicit horizontal eddy viscosity ( $K_{MH}$ ). Fig. 16 shows the time evolution of BPE\* using a set of values for  $K_{MH}$ , while keeping all the other parameters consistent with experiment le-10-ke-10<sup>3</sup>. The  $K_{MH}$  values were set to  $1.12 \times 10^{-1}$ ,  $1.60 \times 10^{-2}$ ,  $1.12 \times 10^{-2}$  and  $0 \text{ m}^2 \text{ s}^{-1}$  corresponding to  $Re_H$  values of 100, 700, 1000 and implicit (i.e., entirely controlled by the implicit numerical diffusion), respectively. Initially (until  $t^* = 2$ ) all the cases display similar results, but then an increase in BPE\* (or mixing) is achieved by decreasing  $K_{MH}$  (or by increasing  $Re_H$ ). Note that although  $Re_H$  is taken to infinity (by setting  $K_{MH} = 0 \text{ m}^2/\text{s}$ ) the effective  $Re$  remains finite because of the implicit numerical diffusion.

## References

- Baumert, H., Peters, H., 2004. Turbulence closure, steady state, and collapse into waves. *J. Phys. Oceanogr.* 34, 505–512.
- Baumert, H., Simpson, J., Sündermann, J., 2005. Marine Turbulence. Cambridge University Press, Cambridge, UK.
- Berselli, L., Fischer, P., Iliescu, T., Özgökmen, T., 2011. Horizontal approximate deconvolution for stratified flows: analysis and computations. *J. Sci. Comput.* 49, 3–20.
- Boccaletti, G., Ferrari, R., Fox-Kemper, B., 2007. Mixed layer instabilities and restratification. *J. Phys. Oceanogr.* 37, 2228–2250.
- Botelho, D., Imberger, J., Dallimore, C., Hodges, B., 2009. A hydrostatic/non-hydrostatic grid-switching strategy for computing high-frequency, high wave number motions embedded in geophysical flows. *Env. Modell. Softw.* 24, 473–488.
- Boyd, J.P., 2001. Chebyshev and Fourier Spectral Methods. Courier Dover Publications.
- Burchard, H., Baumert, H., 1995. On the performance of a mixed-layer model based on the  $k - \epsilon$  turbulence closure. *J. Geophys. Res.* 100, 8523–8540.
- Burchard, H., Bolding, K., 2001. Comparative analysis of four second-moment turbulence closure models for the oceanic mixed layer. *J. Phys. Oceanogr.* 31, 1943–1968.
- Calil, P.H.R., Richards, K.J., 2010. Transient upwelling hot spots in the oligotrophic North Pacific. *J. Geophys. Res.* 115, 1–20.
- Campin, J.M., Hill, C., Jones, H., Marshall, J., 2010. Super-parameterization in ocean modeling: application to deep convection. *Ocean Modell.* 36, 90–101.
- Canuto, V.M., Howard, A., Cheng, Y., Dubovikov, M.S., 2001. Ocean turbulence. Part I: One-point closure model momentum and heat vertical diffusivities. *J. Phys. Oceanogr.* 31, 1413–1426.
- Canuto, V., Cheng, Y., Howard, A., 2007. Non-local ocean mixing mode and a new plume model for deep convection. *Ocean Modell.* 16, 28–46.
- Capet, X., McWilliams, J.C., Molemaker, M.J., Shchepetkin, A.F., 2008. Mesoscale to Submesoscale transition in the California current system. Part I: flow structure, eddy flux, and observational tests. *J. Phys. Oceanogr.* 38, 29–43.
- Cerovečki, I., Plumb, R.A., Heres, W., 2009. Eddy transport and mixing in a wind-and buoyancy-driven jet on the sphere. *J. Phys. Oceanogr.* 39,
- Chang, Y.S., Xu, X., Özgökmen, T.M., Chassignet, E.P., Peters, H., Fischer, P.F., 2005. Comparison of gravity current mixing parameterizations and calibration using a high-resolution 3D nonhydrostatic spectral element model. *Ocean Modell.* 10, 342–368.
- Chang, Y.S., Özgökmen, T.M., Peters, H., Xu, X., 2008. Numerical simulation of the red sea outflow using HYCOM and comparison with REDSOX observations. *J. Phys. Oceanogr.* 38, 337–358.
- Chassignet, E., Hurlbut, H., Smedstad, O., Halliwell, G., Hogan, P., Wallcraft, A., Bleck, R., 2006. Ocean prediction with the hybrid coordinate ocean model (HYCOM). *Ocean Weather Forecasting* 5, 413–426.
- Debreu, L., Marchesiello, P., Penven, P., Cambon, G., 2012. Two-way nesting in split-explicit ocean models: algorithms, implementation and validation. *Ocean Modell.* 49–50, 1–21.
- Dong, C., McWilliams, J.C., Shchepetkin, A.F., 2007. Island wakes in deep water. *J. Phys. Oceanogr.* 37, 962–981.
- Duan, J., Fischer, P., Iliescu, T., Özgökmen, T., 2010. Bridging the Boussinesq and primitive equations through spatio-temporal filtering. *Appl. Math. Lett.* 23, 453–456.
- Eldevik, T., Dysthe, K., 2002. Spiral eddies. *J. Phys. Oceanogr.* 32, 851–869.
- Fischer, P., 1997. An overlapping Schwarz method for spectral element solution of the incompressible Navier-Stokes equations. *J. Comput. Phys.* 133, 84–101.
- Fischer, P., Ho, L.W., Karniadakis, G.E., Ronquist, E.M., Patera, A.T., 1988. Recent advances in parallel spectral element simulation of unsteady incompressible flows. *Comput. Struct.* 30, 217–231.
- Fox-Kemper, B., Ferrari, R., 2008. Parameterization of mixed layer eddies. Part II: prognosis and impact. *J. Phys. Oceanogr.* 38, 1166–1179.
- Fox-Kemper, B., Menemenlis, D., 2008. Can large eddy simulation techniques improve mesoscale rich ocean models? *Geophys. Monogr. Ser.*, 319–337.
- Fox-Kemper, B., Ferrari, R., Hallberg, R., 2008. Parameterization of mixed layer eddies. Part I: theory and diagnosis. *J. Phys. Oceanogr.* 38, 1145–1165.
- Fringer, O., Gerritsen, M., Street, R., 2006. An unstructured-grid, finite-volume, nonhydrostatic, parallel coastal ocean simulator. *Ocean Modell.* 14, 139–173.
- Griffies, S.M., 2004. Fundamentals of Ocean Climate Models. 1, vol. 518. Princeton University Press.
- Griffies, S., Böning, C., Bryan, F., Chassignet, E., Gerdes, R., Hasumi, H., Hirst, A., Treguier, A., Webb, D., 2000. Developments in ocean climate modelling. *Ocean Modell.* 2, 123–192.
- Haidvogel, D., Arango, H., Budgell, W., Cornuelle, B., Curchitser, E., Di Lorenzo, E., Fennel, K., Geyer, W., Hermann, A., Lanerolle, L., 2008. Ocean forecasting in terrain-following coordinates: Formulation and skill assessment of the Regional Ocean Model System. *J. Comput. Phys.* 227, 3595–3624.
- Hamlington, P.E., Van Roekel, L.P., Fox-Kemper, B., Julien, K., Chini, G.P., 2014. Langmuir-submesoscale interactions: Descriptive analysis of multiscale frontal spin-down simulations. *J. Phys. Oceanogr.* 44, 2249–2272.
- Hodges, B.R., Laval, B., Wadzuk, B.M., 2006. Numerical error assessment and a temporal horizon for internal waves in a hydrostatic model. *Ocean Modell.* 13, 44–64.
- Hurlburt, H.E., Chassignet, E.P., Cummings, J.A., Kara, A.B., Metzger, E.J., Shriver, J.F., Smedstad, O.M., Wallcraft, A.J., Barron, C.N., 2008. Eddy-resolving global ocean prediction. *Ocean Modell. Eddying Regime.* AGU Monograph, 3523–382.
- Hurlburt, H.E., Brassington, G.B., Drillet, Y., Kamachi, M., Benkiran, M., Bourdalle-Badie, R., Chassignet, E.P., Jacobs, G.A., Galloudec, O.L., Lellouche, J.M., Metzger, E.J., Smedstad, O.M., Wallcraft, A.J., 2009. High-resolution global and basin-scale ocean analyses and forecasts. *Oceanography* 3, 110–127.
- Ilicak, M., Özgökmen, T., Peters, H., Baumert, H., Iskandarani, M., 2008. Performance of two-equation turbulence closures in three-dimensional simulations of the Red Sea overflow. *Ocean Modell.* 24, 122–139.
- Ilicak, M., Özgökmen, T.M., Özsoy, E., Fischer, P.F., 2009. Non-hydrostatic modeling of exchange flows across complex geometries. *Ocean Modell.* 29, 159–175.
- Ilicak, M., Adcroft, A.J., Griffies, S.M., Hallberg, R.W., 2012. Spurious diurnal mixing and the role of momentum closure. *Ocean Modell.* 45–46, 37–58.
- Inall, M.E., Aleynik, D., Neil, C., 2013. Horizontal advection and dispersion in a stratified shelf sea: the role of inertial oscillations. *Prog. Ocean.* 117, 25–36.
- Kanarska, Y., Shchepetkin, A., McWilliams, J., 2007. Algorithm for non-hydrostatic dynamics in the regional oceanic modeling system. *Ocean Modell.* 18, 143–174.
- Kantha, L.H., Clayton, C.A., 1994. An improved mixed layer model for geophysical applications. *J. Geophys. Res.* 99, 252355–25266.
- Kantha, L.H., Clayton, C.A., 2000. Numerical Models of Oceans and Oceanic Processes. Academic Press.
- Klein, P., Lapeyre, G., 2009. The oceanic vertical pump induced by mesoscale and submesoscale turbulence. *Annu. Rev. Mar. Sci.* 1, 351–375.
- Large, W.G., 1998. Modeling and parameterizing the ocean planetary boundary layer. *Ocean Modelling and Parameterization.* Springer, 81–120.
- Large, W., McWilliams, J., Doney, S., 1994. Oceanic vertical mixing: a review and a model with a nonlocal boundary layer parameterization. *Rev. Geophys.* 32, 363–403.
- Legg, S., Ezer, T., Jackson, L., Briegleb, B., Danabasoglu, G., Large, W., Wu, W., Chang, Y., Özgökmen, T.M., Peters, H., Xu, X., Chassignet, E.P., Gordon, A.L., Griffies, S., Hallberg, R., Price, J., Riemenschneider, U., Yang, J., 2009. Improving oceanic overflow representation in climate models: the gravity current entrainment climate process team. *Bull. Am. Meteor. Soc.* 90, 657–670.
- Lemarié, F., Kurian, J., Shchepetkin, A.F., Jeroen Molemaker, M., Colas, F., McWilliams, J.C., 2012. Are there insurmountable issues prohibiting the use of terrain-following coordinates in climate models? *Ocean Modell.* 42, 57–79.
- Lévy, M., Klein, P., Treguier, A.M., 2001. Impact of sub-mesoscale physics on production and subduction of phytoplankton in an oligotrophic regime. *J. Mar. Res.* 59, 535–565.
- MacCready, P., Banas, N.S., Hickey, B.M., Dever, E.P., Liu, Y., 2009. A model study of tide- and wind-induced mixing in the Columbia River Estuary and plume. *Cont. Shelf Res.* 29, 278–291.
- Mahadevan, A., Tandon, A., 2006. An analysis of mechanisms for submesoscale vertical motion at ocean fronts. *Ocean Modell.* 14, 241–256.
- Mahadevan, A., Tandon, A., Ferrari, R., 2010. Rapid changes in mixed layer stratification driven by submesoscale instabilities and winds. *J. Geophys. Res.* 115, 1–12.
- Marshall, J., Jones, H., Hill, C., 1998. Efficient Ocean Modell. using non-hydrostatic algorithms. *J. Mar. Syst.* 18, 115–134.
- Martin, P., Book, J., Burrage, D., Rowley, C., Tudor, M., 2009. Comparison of model-simulated and observed currents in the central Adriatic during DART. *J. Geophys. Res.* 114. <http://dx.doi.org/10.1029/2008JC004842>.
- McWilliams, J., 1985. A uniformly valid model spanning the regimes of geostrophic and isotropic, stratified turbulence: balanced turbulence. *J. Atmos. Sci.* 42, 1773–1774.
- McWilliams, J.C., 1985. Submesoscale, coherent vortices in the ocean. *Rev. Geophys.* 23, 165–182.
- McWilliams, J.C., 2008. Fluid dynamics at the margin of rotational control. *Environ. Fluid Mech.* 8, 441–449.
- McWilliams, J.C., Sullivan, P.P., Moeng, C.H., 1997. Langmuir turbulence in the ocean. *J. Fluid Mech.* 334, 1–30.
- Mellor, G.L., Yamada, T., 1982. Development of a turbulence closure model for geophysical fluid problems. *Rev. Geophys.* 30, 851–875.
- Müller, P., McWilliams, J., Molemaker, M., 2005. Routes to dissipation in the ocean: the two-dimensional/three-dimensional turbulence conundrum. In: Baumert, H.Z., Simpson, J., Sündermann, J. (Eds.), *Marine Turbulence: Theories, Observations, and Models, Results of the CARTUM Project*. University Press, pp. 397–405.
- Özgökmen, T., Fischer, P., 2012. CFD application to oceanic mixed layer sampling with Lagrangian platforms. *Int. J. Comput. Fluid. Dyn.* 26, 337–348.

- Özgökmen, T.M., Johns, W., Peters, H., Matt, S., 2003. Turbulent mixing in the Red Sea outflow plume from a high-resolution nonhydrostatic model. *J. Phys. Oceanogr.* 33, 1846–1869.
- Özgökmen, T.M., Iliescu, T., Fischer, P., Srinivasan, A., Duan, J., 2007. Large eddy simulation of stratified mixing in two-dimensional dam-break problem in a rectangular enclosed domain. *Ocean Modell.* 16, 106–140.
- Özgökmen, T., Iliescu, T., Fischer, P., 2009a. Large eddy simulation of stratified mixing in a three-dimensional lock-exchange system. *Ocean Modell.* 26, 134–155.
- Özgökmen, T., Iliescu, T., Fischer, P., 2009b. Reynolds number dependence of mixing in a lock-exchange system from direct numerical and large eddy simulations. *Ocean Modell.* 30, 190–206.
- Özgökmen, T., Poje, A., Fischer, P., Haza, A., 2011. Large eddy simulations of mixed layer instabilities and sampling strategies. *Ocean Modell.* 39, 311–331.
- Özgökmen, T., Poje, A., Fischer, P., Childs, H., Krishnan, H., Garth, C., Haza, A., Ryan, E., 2012. On multi-scale dispersion under the influence of surface mixed layer instabilities and deep flows. *Ocean Modell.* 56, 16–30.
- Patera, A., 1984. A spectral element method for fluid dynamics: laminar flow in a channel expansion. *J. Comput. Phys.* 54, 468–488.
- Peters, H., Gregg, M., Toole, J., 1988. On the parameterization of equatorial turbulence. *J. Geophys. Res.: Oceans (1978–2012)* 93, 1199–1218.
- Piggott, M., Gorman, G., Pain, C., Allison, P., Candy, A., Martin, B., Wells, M., 2008. A new computational framework for multi-scale ocean modelling based on adapting unstructured meshes. *Int. J. Numer. Methods Fluids* 56, 1003–1015.
- Plumb, R.A., Ferrari, R., 2005. Transformed Eulerian-mean theory. Part I: nonquasigeostrophic theory for eddies on a zonal-mean flow. *J. Phys. Oceanogr.* 35.
- Prather, M.J., 1986. Numerical advection by conservation of second-order moments. *J. Geophys. Res.: Atmos.* (1984–2012) 91, 6671–6681.
- Ramachandran, S., Tandon, A., Mahadevan, A., 2013. Effect of subgrid-scale mixing on the evolution of forced submesoscale instabilities. *Ocean Modell.* 66, 45–63.
- Sagaut, P., 2006. Large eddy simulation for incompressible flows. Scientific Computation. Springer-Verlag, Berlin.
- San, O., Staples, A., Wang, Z., Iliescu, T., 2011. Approximate deconvolution large eddy simulation of a barotropic ocean circulation model. *Ocean Modell.* 40, 120–132.
- Scotti, A., Mitran, S., 2008. An approximated method for the solution of elliptic problems in thin domains: application to nonlinear internal waves. *Ocean Modell.* 25, 144–153.
- Shchepetkin, A.F., McWilliams, J.C., 1998. Quasi-monotone advection schemes based on explicit locally adaptive dissipation. *Mon. Weather Rev.* 126, 1541–1580.
- Shchepetkin, A.F., McWilliams, J.C., 2005. The regional oceanic modeling system (ROMS): a split-explicit, free-surface, topography-following-coordinate oceanic model. *Ocean Modell.* 9, 347–404.
- Song, Y., Haidvogel, D.B., 1994. A semi-implicit ocean circulation model using a generalized topography-following coordinate system. *J. Comput. Phys.* 115, 228–244.
- Sundermeyer, M., Ledwell, J., 2001. Lateral dispersion over the continental shelf: analysis of dye release experiments. *J. Geophys. Res.* 106, 9603–9621.
- Tandon, A., Garrett, C., 1994. Mixed layer restratification due to a horizontal density gradient. *J. Phys. Oceanogr.* 24, 1419–1424.
- Taylor, J.R., Ferrari, R., 2009. On the equilibration of a symmetrically unstable front via a secondary shear instability. *J. Fluid Mech.* 622, 103–113.
- Thomas, L., Tandon, A., Mahadevan, A., 2008 . Submesoscale processes and dynamics. Eddy resolving ocean models. *Geophysical Monograph*, vol. 177, pp. 17–38.
- Thompson, P.G., Richman, J.G., Hogan, P.J., 2011. Energetics of a global ocean circulation model compared to observations. *Geophys. Res. Lett.* 38, 12–17.
- Tseng, Y.H., Ferziger, J.H., 2001. Mixing and available potential energy in stratified flows. *Phys. Fluids* 13, 1281.
- Umlauf, L., Burchard, H., 2005. Second-order turbulence closure models for geophysical boundary layers. A review of recent work. *Cont. Shelf Res.* 25, 795–827.
- Vallis, G., 2006. Atmospheric and Oceanic Fluid Dynamics. Cambridge University Press.
- Wang, D., McWilliams, J.C., Large, W.G., 1998. Large-eddy simulation of the diurnal cycle of deep equatorial turbulence. *J. Phys. Oceanogr.* 28, 129–148.
- Warner, J.C., Geyer, W.R., Lerczak, J.A., 2005a. Numerical modeling of an estuary: a comprehensive skill assessment. *J. Geophys. Res.* 110.
- Warner, J.C., Sherwood, C.R., Arango, H.G., Signell, R.P., 2005b. Performance of four turbulence closure methods implemented using a generic length scale method. *Ocean Modell.* 8, 81–113.
- Wilcox, D., 1998. Turbulence Modeling for CFD,. DCW Industries Inc.
- Winters, K.B., Lombard, P.N., Riley, J.J., D'Asaro, E.A., 1995. Available potential energy and mixing in density-stratified fluids. *J. Fluid Mech.* 289, 115.
- Xu, X., Chang, Y., Peters, H., Özgökmen, T., Chassignet, E., 2006. Parameterization of gravity current entrainment for ocean circulation models using a high-order 3D nonhydrostatic spectral element model. *Ocean Modell.* 14, 19–44.